

1 **Antarctic ocean and sea ice response to ozone depletion: a two**
2 **timescale problem**

3 DAVID FERREIRA, * JOHN MARSHALL,

Department of Earth, Atmospheric and Planetary Sciences, Massachusetts Institute of Technology, Cambridge, MA

4 CECILIA M. BITZ,

Atmospheric Sciences Department, University of Washington, Seattle, WA

5 SUSAN SOLOMON, AND ALAN PLUMB

Department of Earth, Atmospheric and Planetary Sciences, Massachusetts Institute of Technology, Cambridge, MA

* *Corresponding author address:* David Ferreira, now at the Department of Meteorology, University of Reading, PO Box 243, Reading, RG6 6BB, UK.

E-mail: d.g.ferreira@reading.ac.uk

ABSTRACT

7 The response of the Southern Ocean to a repeating seasonal cycle of ozone loss is studied
8 in two coupled climate models and found to comprise both fast and slow processes. The
9 fast response is similar to the inter-annual signature of the Southern Annular Mode (SAM)
10 on Sea Surface Temperature (SST), on to which the ozone-hole forcing projects in the sum-
11 mer. It comprises enhanced northward Ekman drift inducing negative summertime SST
12 anomalies around Antarctica, earlier sea ice freeze-up the following winter, and northward
13 expansion of the sea ice edge year-round. The enhanced northward Ekman drift, however,
14 results in upwelling of warm waters from below the mixed layer in the region of seasonal sea
15 ice. With sustained bursts of westerly winds induced by ozone-hole depletion, this warming
16 from below eventually dominates over the cooling from anomalous Ekman drift. The result-
17 ing slow-timescale response (years to decades) leads to warming of SSTs around Antarctica
18 and ultimately a reduction in sea-ice cover year-round. This two-timescale behavior - rapid
19 cooling followed by slow but persistent warming - is found in the two coupled models anal-
20 ysed, one with an idealized geometry, the other a complex global climate model with realistic
21 geometry. Processes that control the timescale of the transition from cooling to warming,
22 and their uncertainties are described. Finally we discuss the implications of our results for
23 rationalizing previous studies of the effect of the ozone-hole on SST and sea-ice extent.

24 1. Introduction

25 The atmospheric circulation over the Southern Ocean (SO) has changed over the past
26 few decades, notably during Austral summer, with the pattern of decadal change closely
27 resembling the positive phase of the Southern Annular Mode (SAM). Throughout the tro-
28 posphere, pressure has trended downward south of 60°S and upward between 30 and 50°S
29 in summer (Thompson and Solomon 2002; Marshall 2003; Thompson et al. 2011). This
30 pattern of pressure change is associated with a poleward shift of the westerly winds. These
31 circulation trends have been attributed in large part to ozone depletion in the stratosphere
32 over Antarctica (Gillett and Thompson 2003; Marshall et al. 2004a; Polvani et al. 2011).
33 During the same period, an expansion of the Southern Hemisphere sea ice cover has been
34 observed, which most studies find to be significant (Zwally et al. 2002; Comiso and Nushio
35 2008; Turner et al. 2009). This expansion is observed in all seasons but is most marked in
36 the fall (March-April-May). This is in stark contrast with the large decrease of Arctic sea
37 ice coverage observed over recent decades (Turner et al. 2009).

38 The ozone-driven SAM and sea ice trends could be related. However, several published
39 studies using coupled climate models consistently show a warming of the SO surface and sea
40 ice loss (in all seasons) in response to ozone depletion (Sigmond and Fyfe 2010; Bitz and
41 Polvani 2012; Smith et al. 2012; Sigmond and Fyfe 2014). These studies concluded that the
42 ozone hole did not contribute significantly to the expansion of the SO sea ice cover over the
43 last three decades (see also review by Previdi and Polvani 2014). This leaves us with an even
44 bigger question: how could the SO sea ice cover increase in the face of both ozone depletion
45 and global warming if both processes induce loss? The quandary is further complicated by
46 the correlation between the SAM and ocean/sea ice variability found in both observations and
47 models (Watterson 2000; Hall and Visbeck 2002; Sen Gupta and England 2006; Ciasto and
48 Thompson 2008). Interannual variability in the SAM has a robust Sea Surface Temperature
49 (SST) signature: a dipole in the meridional direction with a strong zonal symmetry. For a
50 positive phase of the SAM, SST cools around Antarctica (south of about 50°S) and warms

51 around 40°S. This response is understood as one that is mainly forced by Ekman currents
52 and to a lesser extent air-sea fluxes (i.e. mixed layer dynamics). A positive phase of the
53 SAM is also associated with sea ice expansion at all longitudes except in the vicinity of
54 Drake Passage (Lefebvre et al. 2004; Sen Gupta and England 2006; Lefebvre and Goosse
55 2008). Although difficult to measure, the Southern Ocean sea ice cover as a whole appears
56 to increase slightly following a positive SAM. If this were the only important process at
57 work, then one would expect a positive SAM-like atmospheric response to ozone depletion
58 to drive SST cooling and sea ice expansion around Antarctica (and a SST warming around
59 40°S) in the long term. This scenario is reinforced by the clear resemblance between the
60 pattern of sea ice concentration trends and the pattern of the sea ice response to a positive
61 SAM. Following this chain of thought, Goosse et al. (2009) pointed to the ozone-driven SAM
62 changes as the main driver of the observed SO sea ice expansion. This behavior however
63 contradicts results from coupled climate models.

64 In this study, we attempt to reconcile the expectations from the aforementioned observed
65 SAM/SST correlations with those from coupled modeling studies including a representation
66 of ozone depletion. In particular, we compute the transient ocean response to a step func-
67 tion in ozone depletion, but one that includes the seasonal cycle of depletion, in two coupled
68 climate models, the MITgcm and CCSM3.5. As we shall see, this exposes the elemental
69 processes and timescales at work. The approach, in direct analogy to the Climate Response
70 Functions (CRFs) for Greenhouse gas forcing, is described in general terms in Marshall et al.
71 (2014). We find that the SST response to ozone depletion is made up of two phases in both
72 models (as summarized in the schematic in Fig. 1): a (fast) dipole response with a cool-
73 ing around Antarctica (consistent with SAM/SST correlations on interannual timescales),
74 followed by a slow warming at all latitudes south of 30°S. This warming eventually leads
75 to a sign reversal of the SST response around Antarctica, and a switch to a positive SST
76 response throughout the SO, consistent with previous coupled GCM experiments.

77 Concomitant with SST fluctuations around Antarctica, our models display increases in

78 sea ice extent in the cooling phase followed by a decrease as SST warms. The long-term
79 response of SST and sea ice in our models is consistent with the conclusions of previous
80 authors. The short term response, however, suggests that ozone depletion may have con-
81 tributed to the observed sea ice expansion of the last decades (see Marshall et al. 2014).
82 The period during which sea ice could expand in response to ozone depletion depends on
83 the processes that control the timescale of the SST and sea ice reversal. While the reversal
84 occurs in both models, they exhibit a rather disparate timescale of transition from warming
85 to cooling. Reasons for these differences are discussed.

86 Our paper is set out as follows. In section 2, the coupled GCM set-ups and experimental
87 designs are described. The ocean and sea ice responses to an abrupt ozone depletion and their
88 mechanisms in the MITgcm and in CCSM3.5 are described in section 3 and 4, respectively.
89 Using a simple analytical model, in section 5 we identify key processes that account for the
90 different timescales in the two coupled GCMs. Finally, conclusions are given in section 6.

91 **2. Coupled model set-ups**

92 *a. The MITgcm*

93 We use the MITgcm in a coupled ocean-atmosphere-sea ice simulation of a highly ide-
94 alized Earth-like Aquaplanet. Geometrical constraints on ocean circulation are introduced
95 through “sticks” which extend from the top of the ocean to its flat bottom (Marshall et al.
96 2007; Enderton and Marshall 2009; Ferreira et al. 2010) but present a vanishingly small land
97 surface area to the atmosphere above. In the “Double-Drake” configuration employed here,
98 two such sticks separated by 90° of longitude extend from the North Pole to 35°S , defining a
99 small basin and a large basin in the northern hemisphere and a zonally re-entrant Southern
100 ocean. There is no land mass at the South Pole.

101 The atmospheric model resolves synoptic eddies, has a hydrological cycle with a represen-
102 tation of convection and clouds, a simplified radiation scheme and an atmospheric boundary

103 layer scheme (following Molteni 2003). The atmosphere is coupled to an ocean and a ther-
104 modynamic sea-ice model (based on the formulation of Winton (2000)) driven by winds and
105 air-sea heat and moisture fluxes. In the ocean, effects of mesoscale eddies are parametrized
106 as an advective process (Gent and McWilliams 1990) and an isopycnal diffusion (Redi 1982)
107 using an eddy transfer coefficient of $1200 \text{ m}^2 \text{ s}^{-1}$. Convection is parameterized as described
108 in Klinger et al. (1996). The coupled model is integrated forward using the same dynamical
109 core (Marshall et al. 1997a,b, 2004b) on the conformal cubed sphere (Adcroft et al. 2004).
110 In calculations presented here, present-day solar forcing is employed, including a seasonal
111 cycle, with present-day levels of greenhouse gas forcing. More details can be found in the
112 appendix.

113 Despite the idealized continents, Double-Drake’s climate has many similarities with to-
114 day’s Earth (Ferreira et al. 2010). Deep water is formed in the northern part of the narrow
115 Atlantic-like basin and is associated with a deep overturning circulation extending into the
116 Southern Ocean where it upwells isopycnally under the combined action of surface winds and
117 (parameterized) eddies. In contrast, the wide, Pacific-like basin is primarily wind driven. A
118 vigorous current, analogous to the Antarctic Circumpolar Current (ACC) develops in the
119 Southern Hemisphere in thermal wind balance with steep outcropping isopycnals. The sea
120 ice cover is perennial poleward of 75°S , but expands seasonally to about 65°S in September
121 (an increase of about 13.5 millions km^2 in sea ice area), similar to today’s seasonal variations
122 in the Southern Ocean (e.g. Parkinson and Cavalieri 2012). In accord with observations, the
123 simulated ocean stratification south of the ACC is controlled by salinity, with temperature
124 increasing at depth (notably because of the seasonal cycle of sea ice). This temperature in-
125 version will turn out to be a central factor controlling the rate of subsurface warming under
126 seasonal sea ice found in response to SAM forcing.

127 Ozone is not explicitly computed in the model, but its shortwave absorption in the
128 lower stratosphere is represented (the model includes a single layer representing the lower
129 stratosphere). Our ”ozone hole” perturbation is introduced by reducing the ozone-driven

130 shortwave absorption south of 60°S in this layer. The imposed ozone reduction is close to
131 100% at the Oct/Nov boundary as observed in the lower stratosphere but is tapered down
132 to 20% in spring (i.e. there is a minimum ozone depletion of 20% throughout the year).
133 This perturbation is comparable to that observed in the heart of the ozone hole during the
134 mid-to-late 90s (e.g. Solomon et al. 2007). The same perturbation is repeated every year.
135 Note also that the ozone radiative perturbation is scaled by the incoming solar radiation and
136 disappears during the polar night at high-latitudes.

137 The forced response is computed as the difference between the ensemble-average of the
138 perturbed runs and the climatology of a 300 years long control run. Twenty 40-year long sim-
139 ulations with independent initial conditions (in both ocean and atmosphere) taken from the
140 control run are carried out and monthly-mean outputs taken. Eight of those are integrated
141 up to 350 years, by which point the coupled system approaches a new equilibrium.

142 Although our atmospheric model is simplified, it produces an atmospheric response to
143 ozone depletion which is rather similar to that found in more complex atmospheric and
144 coupled GCMs (e.g. Gillet and Thompson 2003; Sigmond et al. 2010; Polvani et al. 2011):
145 pressure decreases poleward of 50°S and increases in the 50-20°S band during the summer.
146 This is illustrated in Fig. 2 (top) where the geopotential height at 500 mb is plotted. The
147 geopotential response vanishes during the winter months. There is an associated strength-
148 ening/weakening of the westerly wind around 50/30°S, as shown in Fig. 3. The amplitude
149 of the anomaly, ± 40 m at 500 mb, is also comparable to those obtained in other studies in
150 response to a mid-1990s ozone depletion (Gillet and Thompson 2003). At the surface, the
151 westerly wind stress anomaly is order 0.02 N m^{-2} at its summer peak corresponding to a sea
152 level pressure response of ± 3 mb, both comparable to those found by Sigmond et al. (2010)
153 and Polvani et al. (2011).

154 Note that, as in other GCMs, the atmospheric response to ozone depletion strongly
155 projects on the dominant mode of atmospheric variability (as defined through an EOF anal-
156 ysis) which resembles the observed SAM. We do not explore the dynamics of this atmospheric

157 response here, but it is linked to a cooling of the lower stratosphere and a seasonal SAM-like
158 tropospheric anomaly. Instead, we focus on the transient response of the ocean and sea-ice
159 to the atmospheric anomalies. But, first, let us describe analogous calculations carried out
160 with the NCAR Community Climate model.

161 *b. CCSM3.5*

162 We use the Community Climate System Model version 3.5 (CCSM3.5) configured as in
163 Gent et al. (2010), Kirtman et al. (2012), Bitz and Polvani (2012), and Bryan et al. (2013).
164 All four studies describe the simulated climate of the CCSM3.5 and the latter two focus
165 on the Southern Ocean and Antarctic sea ice therein. The atmospheric component has a
166 finite-volume dynamical core and a horizontal resolution of $0.47^\circ \times 0.63^\circ$ with 26 vertical
167 levels. The horizontal grid of the land is the same as the atmosphere. The ocean and sea
168 ice have a resolution of nominally 1° . The ocean eddy parameterization employs the Gent
169 and McWilliams (GM) form (as in MITgcm), but with a GM coefficient varying in space
170 and time following Ferreira et al. (2005), as described in Danabasoglu and Marshall (2007).

171 All of our integrations with CCSM3.5 have greenhouse gases and aerosols fixed at 1990s
172 level. The initial conditions were taken from a 1990s control simulation carried out with
173 the CCSM3. The CCSM3.5 was first run for 155 years (see Kirtman et al. 2012) with
174 ozone concentrations intended to be representative of 1990s levels that were prepared for the
175 CCSM3 1990s control integrations (see Kiehl et al. 1999). However, compared to more recent
176 estimates of ozone concentrations from the Atmospheric Chemistry and Climate and Strato-
177 spheric Processes and their Role in Climate (AC&C/SPARC) dataset (Cionni et al. 2011),
178 the CCSM3 estimates for 1990s resemble the level of ozone depletion in the Antarctic strato-
179 sphere of approximately 1980, or about half the level of depletion since preindustrial times.
180 Hence, to create a quasi-equilibrated "high-ozone" control integration, with preindustrial-
181 like ozone concentrations, we ran an integration where we first ramped up the ozone con-
182 centration for the first 20 years by adding a quantity each month equal to one-fortieth of

183 the difference between the decadal mean for the 2000s and 1960s for a given month of the
184 AC&C/SPARC dataset. We then stabilized the ozone concentrations at this 1960s level of
185 the AC&C/SPARC dataset for another 50 years. From the last 30 yrs of this 1960s ozone
186 level simulation, we ran an ensemble of 26 “abrupt low-ozone” integrations. The prescribed
187 ozone perturbation is equal to the seasonally-varying 2000s minus 1960s difference from the
188 AC&C/SPARC dataset. At first, six ensemble members were branched on January 1st and
189 ran for 20 yrs. At which point we realized that, to examine the very rapid response seen
190 in the first years, a significantly larger ensemble would be required. To optimize resources,
191 these perturbed experiments were started just before the summer season, rather than in the
192 midst of it. Therefore, we ran another twenty ensemble members, branched on September
193 1st and run for 32 months. We use the six longer members to investigate behavior only
194 beyond the first 32 months.

195 Twenty of the ensemble members, with an annual cycle as in the MITgcm, were branched
196 on September 1st and ran for 32 months, and six of the ensemble members were branched
197 on January 1st and ran for 20 years.

198 As in the MITgcm, the atmospheric response to ozone depletion in CCSM3.5 is a positive
199 SAM-like pattern with a maximum amplitude in Dec-Jan-Feb (Fig. 2, bottom). The pattern
200 is similar to that found in other models (see Thompson et al. 2011) albeit with stronger
201 zonal asymmetries, notably marked by a large trough centered on 90°W. At the peak of
202 the summer response, geopotential height anomalies at 500 mb are about ± 20 m, somewhat
203 weaker than those seen in the MITgcm. At the surface, however, sea level pressure anomalies
204 are typically ± 3 mb and are associated with surface wind anomalies of about 1 m s^{-1} (see
205 Bitz and Polvani 2012), similar to those in the MITgcm. Given the differences between
206 the two coupled models, their surface responses to ozone depletion are remarkably similar
207 although the response in CCSM3.5 has larger zonal asymmetries.

208 In the zonal-mean, the wind stress responses of the two models are similar in shape
209 and magnitude although they are shifted relative to one another in latitudinal direction

210 (Fig. 3). For comparison, the surface wind stress difference between "peak-ozone-hole" and
211 "pre-ozone hole" conditions, estimated from the ERA-Interim reanalysis (Dee et al. 2011),
212 is shown in solid. The two models' responses fall on both sides of the change found in the
213 reanalysis. Son et al. (2010) and Sigmond and Fyfe (2014) found a relationship between the
214 tropospheric response to ozone depletion and the location of the climatological jet in models
215 participating, respectively, to the CCMVal-2 and CMIP5 inter-comparison projects. We do
216 not find such relationships here, except that the locations of the peak responses and those
217 of the mean jets are arranged latitudinally in the same sequence. In particular, there is no
218 indication that the magnitude of the response correlates with the mean jet position. Also,
219 despite its realistic mean jet stream, the response of CCSM3.5's sits further away from the
220 reanalysis change than that of the MITgcm. These differences could reflect the differences
221 in the representation of the ozone hole in the two models as well as differences in their mean
222 states and internal dynamics linking the stratospheric cooling to the surface wind stress
223 response. We emphasize that the correlations found by Son et al. (2010) and Sigmond and
224 Fyfe (2014) are extracted from tens of models, but exhibit significant scatter; our small
225 sampling here makes it difficult to draw robust conclusions.

226 **3. Ocean and Sea ice response in the MITgcm**

227 *a. The evolution of the transient SST response*

228 Following the atmospheric response to ozone depletion, the ocean and sea ice cover adjust
229 to the changing winds (Fig. 4). The early (years 0-5) SST response consists of a zonally
230 symmetric dipole: a cooling between 50 and 70°S and a warming in the band 50-25°S
231 (there is also a weak cooling north of 25°S). This initial SST response is of significant
232 magnitude, typically $\pm 0.3^\circ\text{C}$, and is nearly identical to the SST signature of a positive SAM
233 on interannual timescales seen in the MITgcm and similar to that seen in observations and
234 other coupled GCMs (see, e.g. Watterson 2000; Hall and Visbeck 2002; Ciasto and Thompson

235 2008). It is primarily generated by anomalous Ekman currents (see below). After two decades
236 or so, the SST response changes noticeably (Fig. 4, bottom left). The warm pole (50-30°S)
237 has nearly doubled in magnitude while the cold pole has weakened.

238 The ocean response is not limited to the surface (Fig. 4, right). Temperatures at 170 m
239 exhibit a widespread warming south of 30°S with a peak around 40°S, with a slight cooling
240 north of 30°S. The pattern of the subsurface response does not change over time but exhibits,
241 as at the surface, a warming tendency at all latitudes south of 30°S. After 2 decades, the
242 subsurface temperature peaks markedly at two latitudes, 40 and 60°S, where the anomalies
243 reach up to 0.8°C, comparable in strength to the SST anomalies.

244 A continuous monitoring of the SST evolution over the first 40 years after the "ozone
245 hole" inception shows that the initial dipole SST response (south of 25°S) slowly morphs
246 into a warming (Fig. 5, top). By year 40, the character of the SST response more closely
247 mirrors the subsurface temperature pattern than the early SST response. It is notable that
248 the long term SST adjustment (30 years and longer) is similar to that found by Sigmond
249 and Fyfe (2010) and Bitz and Polvani (2012) in response to ozone depletion. These previous
250 studies did not present or discuss the time evolution of the ocean response. Sigmond and
251 Fyfe (2010) carried out 100 year perturbation/control experiments and defined the response
252 to ozone depletion as the 100-y averaged difference between the perturbed and control runs
253 although they mention that the sea ice extent response in their model reaches equilibrium
254 within 5 years. Bitz and Polvani (2012) carried out perturbation experiments in which the
255 ozone hole was ramped up for 20 years and then maintained for an additional 30 years. They
256 defined the response to ozone depletion as the difference between perturbed and control runs
257 averaged over the last 30 years of integration. Clearly, in both cases, the responses were
258 largely dominated by the long (multi-decadal) adjustments of the model ocean to ozone
259 depletion.

260 Our results, however, suggest that there are two phases in the SST response: a fast re-
261 sponse which has a dipole pattern, consistent with expectations from SAM/SST correlations

262 on interannual timescales, followed by a slow widespread warming of the SO similar to results
263 from previous GCMs studies. The transition between the two phases is seen after about 20
264 years in the MITgcm, when the initial cold SST response in the band 50-70°S transitions to
265 warming. SST variations in this band are particularly important because it coincides with
266 the region of seasonal sea ice fluctuations.

267 A closer look at the time evolution of the SST in the band 50-70°S is shown in Fig. 6.
268 The area-averaged SST falls by -0.3°C within a year and then slowly and almost linearly
269 rises to cross zero around year 20. The SST increases for 200 years or so approaching a new
270 equilibrium which is 1.5°C warmer than in the control run (not shown). Ozone depleting
271 substances are no longer being emitted, so in the real world this forcing will not be present
272 long enough for such a response to be realized. It is computed here to illustrate physical
273 processes.

274 Despite the 20-member ensemble, significant noise remains in the ensemble mean area-
275 averaged SST due to internal variability. The grey shading and solid black line in Fig. 6
276 give a measure of the uncertainties in the time evolution of the SST¹. This suggests that the
277 fast SST response ranges between -0.1 and -0.4°C while the time of the sign reversal varies
278 between 15 and 30 years.

279 In concert with SST changes around 70-50°S, the sea ice area also significantly evolves in
280 response to ozone depletion (Fig. 7). As expected, sea ice expands in the presence of colder
281 SSTs and retreats when SSTs become positive, after about 20 years. This increase is seen
282 in all seasons but is largest in winter when sea ice extent is at its peak. Note that the cold
283 SST response is largest in summer when the atmospheric perturbations is the strongest but
284 persists throughout the year (see Fig. 5). The sea ice perturbations are small but significant,
285 representing typically a few percent of the climatological seasonal change.

¹They are computed as follows: 20x8 realizations of the SST response are constructed by forming all possible combinations of one the 20 short runs (year 0-40) with one of the 8 long runs (year 41-350). Each evolution is then fitted to a two timescale exponential form (see Eq. (8) below). The solid black line is the mean of these 160 evolutions while the grey shading indicates plus or minus one standard deviation.

286 *b. Role of interior ocean circulation in SST evolution*

287 We now address the mechanisms that drive the evolution of the SST response.

288 1) THE FAST RESPONSE

289 On short (\sim year) timescales the ocean response is essentially confined to the mixed
290 layer. The SST dipole is primarily forced by Ekman current anomalies due to the SAM-like
291 surface wind response (Fig. 4). South of 45°S , increased surface westerly winds result in
292 an anomalous northward Ekman flow which advects cold water from the South. North of
293 45°S , the opposite happens. The SST tendency due to this forcing, $v'\partial_y\bar{T}$, is plotted in
294 Fig. 8 (dashed-dotted) along with the SST response (red, both averaged over year 2-5).
295 Here, $\partial\bar{T}/\partial y$ is taken from the control, while the full anomalous Eulerian currents v' , not
296 just its Ekman component, are used in the computation. For convenience, the tendency is
297 expressed in W m^{-2} taking a sea water density ρ_o of 1030 kg m^{-3} , a water heat capacity C_p
298 of $3996 \text{ J kg}^{-1} \text{ K}^{-1}$, and a constant mixed layer depth h_s of 30 m (the thickness of the top
299 model level). The pattern of anomalous advection tendency closely matches that of the SST
300 dipole and is of the correct magnitude to explain the SST response (except north of 25°S
301 where vertical advection is an important forcing, see below).

302 In contrast, the net air-sea flux anomaly F' (dominated by the latent contribution, posi-
303 tive downward) damps the SST anomaly to the atmosphere (Fig. 8, solid black). Net air-sea
304 heat fluxes and horizontal advection term (dashed-dotted) closely oppose one another over
305 the first few years. The initial SST dipole is thus the quasi-equilibrium response to the fast
306 mixed layer dynamics:

$$\frac{\partial T'}{\partial t} \simeq -v'\partial_y\bar{T} + F'_a - \lambda T' \simeq 0. \quad (1)$$

307 where the net air-sea heat flux anomaly F' is made up of two contributions: a term F'_a
308 driven by changes in the atmospheric state (independent of SST anomalies, e.g. surface
309 wind changes, shortwave changes) and a SST damping term that varies linearly with T' on

310 a timescale λ^{-1} (positive λ implies a damping to the atmosphere). The fast SST response
311 to ozone depletion in the MITgcm is similar to the SST signature of a positive phase of
312 the SAM in the same model (and similar to the signature found in observations and other
313 models (Ciasto and Thompson 2008; Sen Gupta and England 2006)). Because our set-up
314 is strongly zonally symmetric, the SST forcing is largely dominated by meridional Ekman
315 advection. Note, however, that in more realistic configurations air-sea fluxes due to zonal
316 asymmetries of the SAM pattern may be important locally (Ciasto and Thompson 2008;
317 Sallée et al. 2010).

318 2) THE SLOW RESPONSE

319 The Ekman current anomalies are divergent and drive anomalous upwelling south of 50°S
320 and north of 35°S and an anomalous downwelling between these two latitudes. The Eulerian
321 MOC response consists then of two cells closely matching the surface wind stress anomalies
322 (Fig. 9). South of 35°S where there are no meridional boundaries, the Eulerian MOC
323 streamlines are vertical in the interior (as expected in the geostrophic limit) with return
324 flows in the top and bottom Ekman layers. North of 35°S , meridional barriers allow for a
325 mid-depth geostrophic return flow. At all latitudes, however, the strength of the Eulerian
326 MOC just below the Ekman layer is very well approximated by the theoretical prediction
327 $\tau_x/(\rho_o f)$ (on monthly and longer timescales) where τ_x is the zonal mean zonal wind stress
328 and f the Coriolis parameter (not shown).

329 Anomalies of the residual-mean circulation (sum of the Eulerian and parameterized eddy-
330 induced circulations) are plotted in Fig. 10. Comparison of Figs. 10b and 9 (same averaging
331 periods) shows that the residual-mean MOC anomalies are dominated by the Eulerian flow,
332 retaining a clear connection to the pattern of surface wind anomalies. However, in anal-
333 ogy with the mean state balance, the eddy-induced MOC anomalies tend to oppose the
334 wind-driven circulation anomalies, particularly south of 35°S where there are no meridional
335 barriers. As a result, the residual-mean MOC anomalies are weaker than the wind-driven

336 Eulerian MOC anomalies by as much as a factor two. On average over the band 70-50°S,
 337 the residual-mean upwelling response is about 1 m year⁻¹, compared to 1.5 m year⁻¹ for the
 338 Eulerian component (Fig. 11, top left). Note that the cancellation of the Eulerian vertical
 339 velocity by the eddy-induced component is similar at all depths.

340 Because ocean temperature increases upward north of 55°S (see color contoured in Fig. 9,
 341 bottom), the downwelling and upwelling at these latitudes are expected to result in warming
 342 and cooling, respectively. However, the near-surface temperature stratification south of 55°S
 343 is reversed, with warmer water at depth because of the presence of seasonal sea ice (Fig. 9,
 344 bottom). Then, upwelling south of this limit results in a warming. This is indeed observed in
 345 subsurface layers as shown in Fig. 10. Meridionally, the maximum temperature responses are
 346 clearly associated with branches of upwelling/downwelling. In the vertical, the temperature
 347 response peaks just below the mixed layer, around 100-200 m, where the summertime vertical
 348 stratification $\partial\bar{T}/\partial z$ is the largest. This is within reach of the wintertime deepening of
 349 the mixed layer which, on average in the band 70-50°S, extends to about 150 m at its
 350 deepest. The cold SST response between 70 and 50°S stands out over years 1-5, when
 351 subsurface temperature anomalies remain weak (Fig. 10a). As time increases, however, the
 352 subsurface temperature anomalies grow larger and larger and eventually imprint themselves
 353 into the surface layer, through entrainment, so that by years 21-25, the cold SST anomaly
 354 has disappeared.

355 As shown in Fig. 10d, the time evolution of the subsurface (170 m deep) temperature
 356 response around 60°S is nearly linear over the first 40 years. A best fit gives an average
 357 warming rate of 0.017 °C year⁻¹ (dashed black). This value is readily explained by the
 358 annual mean residual upwelling anomaly w_{res} (~ 1 m year⁻¹) acting on the mean temperature
 359 stratification $\partial\bar{T}/\partial z$ (~ 0.019 °C m⁻¹) at this location. This confirms that the subsurface
 360 temperature response is well approximated by:

$$\frac{\partial T'_{sub}}{\partial t} \simeq -w'_{res} \frac{\partial \bar{T}}{\partial z}. \quad (2)$$

361 How much time is required for the upwelling of warm waters to compensate for the initial

362 cold SST response around 60°S? The fast SST response at 60°S peaks at about -0.4°C (year
 363 3, see Fig. 5, top). Assuming that subsurface temperatures are efficiently carried into the
 364 mixed layer through entrainment, the initial SST response would be cancelled when the
 365 subsurface temperature perturbation reaches +0.4°C. This takes about 20-25 years (Fig.
 366 10d), in good agreement with the SST evolution shown in Fig. 5.

367 After a couple of decades (Fig. 10c), the ocean has warmed south of 30°S at all depths
 368 (due to upwelling/downwelling collocated with positive and negative temperature stratifica-
 369 tion) and cooled north of 30°S (due to upwelling of cold water). This distribution resembles
 370 the averaged responses found by Sigmond and Fyfe (2010) and Bitz and Polvani (2012).
 371 The latter study identifies upwelling/downwelling anomalies driven by the SAM-like atmo-
 372 spheric perturbation as a primary driver of the temperature response. In addition, Bitz and
 373 Polvani (2012) shows (see their Fig. 3) that this effect is at work both at coarse (1°) and
 374 eddy-resolving (0.1°) resolutions in CCSM3.5. Although the relative importance of eddies
 375 and mean flow vertical advection depends on resolution, their result suggests that ocean
 376 eddies do not have a major influence on the quasi-equilibrium response. Note, however, this
 377 does not imply that eddies do not have an influence on the rate at which quasi-equilibrium
 378 response is approached (see below).

379 Two aspects of the temperature evolution deserve comment:

380 1) The fast SST response is driven primarily by anomalous horizontal rather than vertical
 381 advection. A scaling of these two terms is:

$$\alpha = \frac{v'_{res}\bar{T}_y}{w'_{res}\bar{T}_z} \sim \frac{\bar{T}_y L_y}{\bar{T}_z h_s}, \quad (3)$$

382 where \bar{T}_y is the meridional temperature gradient at the surface, \bar{T}_z the stratification just
 383 below the mixed layer, L_y the width of the upwelling zone ($\sim 20^\circ$ for the band 50-70°S).
 384 We assume that, at the scaling level, $v'_{ek}/w'_{ek} \sim v'_{res}/w'_{res}$. We find that α is about 15-
 385 30 (for $\bar{T}_z = -0.015-0.020$ °C m⁻¹, $\bar{T}_y = 4-6 \times 10^{-6}$ °C m⁻¹, and $h_s=30$ m). It is large
 386 because the width of the upwelling zone is much greater than the depth of the horizontal
 387 flow ($L_y \gg h_s$ or equivalently, through volume conservation, $|v'_{ek}| \gg |w'_{ek}|$). Despite the

388 fact that $\overline{T}_z \gg \overline{T}_y$, horizontal advection dominates. In subsurface layers, by contrast, there
 389 are no air-sea fluxes and little damping. Then, subsurface temperature anomalies induced
 390 by anomalous upwelling grow unabated over decades and are eventually imprinted into the
 391 surface layers through entrainment during the fall/winter deepening of the mixed layer.

392 2) The impact of (parameterized) eddies is significant in setting the subsurface warming
 393 rates. As shown above the residual-mean overturning anomalies are dominated by the Eule-
 394 rian wind-driven component on yearly averages but is partially compensated by eddy-induced
 395 MOC anomalies. The anomalous Eulerian component is much larger than the annual mean
 396 during summer months when the anomalous surface wind stress peaks, but is vanishingly
 397 small in winter. By contrast, the eddy-induced circulation anomalies, which are proportional
 398 to the perturbations in isopycnal slope, are more steady. This is reflected in the yearly fluc-
 399 tuations superimposed on the slow increase of the subsurface temperature anomalies at 60°S
 400 shown in Fig. 10d. During summer, the wind forcing dominates and isotherms are lifted.
 401 During wintertime, the wind forcing disappears and only the eddy-induced MOC persists:
 402 isotherms are relaxed back toward their unperturbed position. In the annual mean, the
 403 Eulerian vertical advection dominates, but the rate of temperature increase in subsurface
 404 layers is significantly affected by the eddy contribution. If the wind forcing was the only
 405 process acting, the rate of anomalous upwelling at 60°S would be 2 m year⁻¹, twice as fast
 406 as the rate due to the anomalous residual flow (1 m year⁻¹). Thus, the upwelling anomaly
 407 w'_{res} in Eq. (2) can be expressed as:

$$w'_{res} = \delta w'_{ek} = \delta \frac{\partial}{\partial y} \left(\frac{\tau'_x}{\rho_o f} \right) \quad (4)$$

408 where δ is an "eddy compensation" parameter which ranges from 1 (no eddy compensation)
 409 to 0 (exact eddy compensation). In the MITgcm experiments, $\delta=0.3-0.5$ in the band on
 410 upwelling (70-50°S) at 100-200 m depth. It is interesting that in the mean (i.e. control state)
 411 Eulerian and eddy-induced MOC also compensate roughly by this amount (see Marshall and
 412 Radko 2003).

413 In summary, we find that the warming of SST on long timescales in the band 70-50°S is

414 due to upwelling of warm water (primarily driven by Ekman divergence). The time to the
415 SST reversal is well approximated by the time necessary for the subsurface warming to offset
416 the initial cold SST response, about 20 years here. The long term temperature response is
417 consistent with previous findings and accounts for the retreat of sea ice in response to ozone
418 depletion on long (multidecadal) timescales.

419 **4. Ocean and Sea Ice Response in CCSM3.5**

420 *a. Temperature and sea ice response*

421 The response to ozone depletion in CCSM3.5 has many similarities with that found in
422 the MITgcm, but also some important differences of detail. Of most significance is that
423 the SST response again has two phases: first a dipole response in the meridional direction
424 followed by a widespread warming of the Southern Ocean, as in the MITgcm (Figs. 12 and
425 5, top). CCSM3.5 has much more realistic geometry than the MITgcm configuration and
426 so the initial SST response (similar to the modeled SST signature of a positive phase of
427 the SAM) exhibits important zonal asymmetries, unlike the MITgcm (Fig. 12, top). In
428 particular, the cold SST pole around 60°S is interrupted downstream of the Drake Passage
429 where the warm pole extends across the ACC into the Western part of the Weddel Sea.
430 This feature is also found in the observed SST response to a positive phase of the SAM
431 (see Ciasto and Thompson 2008) and corresponds to a region where air-sea heat fluxes,
432 rather than Ekman currents, dominate the SST anomaly forcing. Note, however, that the
433 SST response to ozone depletion in CCSM3.5 differs from the observed SAM-forced SST
434 anomaly in some other aspects. For example the negative pole in the Pacific sector is larger
435 and extends further equatorward.

436 As in the MITgcm experiment, over time the SST (and subsurface) responses morph into
437 a widespread warming (Fig. 12, bottom). The transition between the two phases however
438 occurs much faster in CCSM3.5, after only 3-5 years (Fig. 5, bottom). Around 60°S, between

439 years 3 and 5, cold SST anomalies during summer (at the peak of the wind forcing) alternate
440 with warm anomalies during winter. At 70°S, the cold SST response reappears during most
441 summers for nearly 2 decades.

442 The amplitude of the SST response in CCSM3.5 is weaker than in the MITgcm, with peak
443 values of $\pm 0.3^\circ\text{C}$ (compared to $\pm 0.6^\circ\text{C}$ in MITgcm), reflecting the difference in the surface
444 wind response to ozone depletion in the two models. Largely due to the zonal asymmetries
445 of the SST response in CCSM3.5, the zonal mean initial response is only -0.2°C (Fig. 5,
446 bottom) and averaged between 70 and 50°S it is only -0.05°C (Fig. 6, right, red solid). For
447 a meaningful comparison with the MITgcm therefore, the SST evolution averaged over the
448 area comprising the initial cold pole (see Fig. 12, top) is also shown in Fig. 6 (right, dashed
449 red). According to this measure, the initial SST response is larger (-0.15°C) in magnitude
450 and changes sign at a later time (5 yr) than in the zonal average. When comparing the two
451 models, the initial cooling response in CCSM3.5 is also partially obscured by the warming
452 trend which grows much more rapidly than in the MITgcm (see below). Despite these
453 differences, the two phases of the SST response are clearly evident in Fig. 6 (right). After
454 the sign reversal during year 3-5, the SST continues to increase for a few years more and
455 appears to stabilize around 0.15°C after a decade or so. Note that only 6 ensemble member
456 are available after 3 years and so larger variability is evident. The appearance of a stationary
457 state after 10 years may not be a robust feature.

458 The rapid transition between the two phases is also evident in the sea ice response. The
459 sea ice area only increases during the first winter following the ozone hole inception (Fig.
460 7, right) while the summer sea-ice area decreases sharply. The area of winter sea-ice also
461 eventually declines. The magnitude of the sea-ice area decline in the slow phase of the two
462 models is similar although the decline occurs about a decade sooner in CCSM3.5.

463 *b. Role of ocean circulation on temperature evolution*

464 The underlying dynamics of the SST evolution in CCSM3.5 is similar to that in the
465 MITgcm although the magnitudes of key terms in the heat budget and implied timescales
466 are different.

467 In the zonal mean, the initial SST anomaly dipole is largely explained by the anomalous
468 Ekman response (Fig. 8, right). To match the short-lived initial response, the forcing terms
469 and SST anomalies in Fig. 8 (right) are averaged over 2 years. The Ekman forcing term (and
470 the SST response) are about half those found in the MITgcm. The air-sea flux anomalies act
471 to damp the SST response at all latitudes. The air-sea flux anomalies and Ekman forcing
472 again tend to balance each other. There is one noticeable exception between 60 and 50°S
473 where the air-sea flux term is larger in magnitude than the Ekman term. Here, the air-sea
474 flux warms the surface faster than it is cooled by Ekman advection. More detailed analysis
475 reveals that this is due to an increased shortwave absorption at the surface due to a decrease
476 of the cloud fraction (not shown).

477 The other important mechanism identified in the MITgcm experiment is the wind-driven
478 subsurface warming below the initial cold SST anomaly. Fig. 11 (right) shows the vertical
479 velocity anomalies and the resulting tendency $-w'_{res} \frac{\partial \bar{T}}{\partial z}$ in CCSM3.5 (at two depths where
480 the values are largest). South of 60°S, the anomalous Ekman divergence drives upwelling in
481 a region where the temperature decreases toward the surface (Fig. 11, top right). As in the
482 MITgcm, this results in a positive tendency. Note that w'_{res} is larger at 70 than at 130 m
483 depth, but that the temperature tendency at 70 m is much smaller because this level lies
484 within the mixed-layer and the temperature stratification is weak. North of 60°S, the mixed
485 layer is shallower and strong tendencies are found closer to the surface. The large positive
486 tendency, of $0.1^{\circ}\text{C year}^{-1}$, centered on 50°S is due to downwelling of warm waters while the
487 large negative tendency around 40°S is due to upwelling of cold water.

488 The vertical advection tendencies in CCSM3.5 are significantly larger than in the MITgcm
489 (Fig. 11, bottom, note the different vertical scales in the two panels), typically by a factor

490 2 in the band 70-50°S (see also estimated values in Table 1 and section 5 below).

491 Comparing the annual- and zonal-mean wind stress responses in the MITgcm and CCSM3.5
492 (Fig. 3), it appears that 1) the responses of the two models are shifted in the meridional di-
493 rection, one with respect to the other (surface wind anomaly peaks around 65°S in CCSM3.5
494 but around 55°S in the MITgcm) and 2) the meridional scale of the wind change in CCSM3.5
495 is smaller than in the MITgcm. This leads to stronger wind curl anomalies and hence larger
496 Eulerian upwelling rates. In addition, the cancellation of the wind driven upwelling by the
497 eddy-induced vertical velocity differs between the two models. In contrast with the MITgcm
498 (Fig. 11, top left), eddy-induced contributions to upwelling rates are very small compared to
499 the Eulerian mean down to 100 m depth in CCSM3.5. The difference in the degree of eddy
500 cancellation between models may be due to differences in the eddy parameterization scheme:
501 the MITgcm uses a constant eddy coefficient while CCSM3.5 uses a temporally and spatially
502 variable eddy coefficient (following Ferreira et al. (2005), see section 2). The combination of
503 a larger wind-driven upwelling and a weaker eddy cancellation largely explains the stronger
504 warming tendencies seen in CCSM3.5 (Fig. 11, bottom), and as we shall see, is a major
505 factor in the shorter cross-over time from cooling to warming.

506 **5. Discussion and development of a simplified model**

507 The discussion in sections 3 and 4 has enabled us to identify common robust mechanisms
508 of warming and cooling in the two models. Here we use the insights gained to present a
509 simplified model of the response of the ocean to SAM forcing which exposes those processes
510 in a transparent way.

511 *a. Formulation*

512 To aid our discussion, motivated by diagnostics of our two coupled models, we present
 513 the following simple model of the temperature response:

$$\frac{\partial T'}{\partial t} = -v'_{res} \frac{\partial \bar{T}}{\partial y} + F'_a - \lambda T' + \Lambda_e T'_{sub} \quad (5)$$

$$\frac{\partial T'_{sub}}{\partial t} = -w'_{res} \frac{\partial \bar{T}_{sub}}{\partial z} - \lambda_{sub} T'_{sub} \quad (6)$$

514 where T' is the SST response, T'_{sub} the subsurface temperature response (imagined to be
 515 typical of the seasonal thermocline) and Λ_e represents the entrainment timescale of the
 516 subsurface temperature into the mixed layer. The subsurface temperature is assumed to
 517 adjust on a timescale λ_{sub}^{-1} which encapsulates complex dynamics relevant to the equilib-
 518 rium response and adjustment of the SO seasonal thermocline. The overbar denotes the
 519 climatological state of the control run, and the prime is the perturbation in response to
 520 the anomalous wind forcing. In the absence of a dynamical response in the ocean interior
 521 ($w'_{res} \simeq 0$) and/or of an influence of the interior on the surface layer ($\Lambda_e = 0$), the SST
 522 anomaly equation reduces to:

$$\frac{\partial T'}{\partial t} = \tilde{F} - \lambda T' \quad (7)$$

523 where $\tilde{F} = F'_a - v'_{res} \partial_y \bar{T}$ is the atmospheric forcing of the mixed layer by air-sea flux and Ek-
 524 man current anomalies. This is the classical model of midlatitude SST variability (Frankig-
 525 noul and Hasselmann 1977).

526 We are interested in the response to a step-function wind change. Assuming a constant
 527 atmospheric forcing ($v'_{res}, w'_{res}, F'_a = \text{const}$) for $t > 0$, solutions are given by:

$$T' \simeq \frac{\tilde{F}}{\lambda} (1 - e^{-\lambda t}) + \frac{\Lambda_e}{\lambda} T'_{sub} \quad (8)$$

$$T'_{sub} = \frac{-w'_{res} \partial_z \bar{T}_{sub}}{\lambda_{sub}} (1 - e^{-\lambda_{sub} t}) \quad (9)$$

528 in the limit $\lambda_{sub} \ll \lambda$ appropriate to our models. The subsurface temperature (9) grows
 529 monotonically on a timescale λ_{sub}^{-1} . The SST response (8) is the sum of two exponential

530 functions: one captures the fast response driven by mixed-layer dynamics while the second
 531 one, $\Lambda_e/\lambda \times T'_{sub}$, is driven by the slow ocean interior dynamics. Note that for $t \ll \lambda_{sub}$, T'_{sub}
 532 increases linearly at a rate given by $-w'_{res} \partial_z \bar{T}_{sub} t$ as found in the coupled GCMs. Parameters
 533 obtained from a best fit of Eqs. (8) and (9) to the SST and subsurface temperature evolution
 534 in both the MITgcm and CCSM3.5 are given in Table 1. The best-fit curves are shown in
 535 Fig. 13 (solid) with their fast and slow components (dashed). It is important to emphasize
 536 that the response to a step function in the classical model (7) reduces to the fast component
 537 if the ocean is passive (lower dashed curves in Fig. 13). Thus both coupled GCMs depart
 538 significantly from the Frankignoul and Hasselmann (1977) classical model, attesting to the
 539 active role of ocean circulation in modulating the SST response.

540 The fitted parameters in Table 1 are clearly estimates and depend on the underlying
 541 assumptions of the simple model Eqs. (5) and (6). They nonetheless provide useful insights
 542 in to processes at work and the differences between the two GCMs. There are two key
 543 differences between the coupled models which we now discuss in turn: air-sea fluxes/damping
 544 rates and the response of the interior ocean.

545 *b. Air-sea interactions*

546 The first difference that stands out is in the strength of the air-sea heat exchanges. The
 547 atmospheric-driven forcing \tilde{F}_F ($= \rho_o C_p h_s \tilde{F}$ in W m^{-2}) is -0.7 W m^{-2} in the MITgcm and
 548 -1.1 W m^{-2} in CCSM3.5 (average values in the band 70-50°S). Comparison with Fig. 8
 549 suggests that \tilde{F}_F largely comprises the anomalous Ekman advection in the MITgcm, but is
 550 significantly amplified by F'_a in CCSM3.5 (possibly because of the larger zonal asymmetries
 551 in CCSM3.5). Changes in the atmospheric circulation (a positive SAM here) and ozone
 552 concentration are both expected to affect the radiation reaching the surface. Recently, Grise
 553 et al. (2013) showed that ozone depletion could alter the top-of-the-atmosphere longwave
 554 and shortwave fluxes by a few W m^{-2} in the band 70-40°S through a modulation of the
 555 cloud fraction. A similar impact on the surface fluxes is anticipated (regardless of the

556 ocean response) although we cannot discriminate between the MITgcm and CCSM3.5 in
557 this respect. In addition, the estimated heat flux feedback $\lambda_F = \lambda/(\rho_o C_p h_s)$ is much larger
558 in CCSM3.5 than in the MITgcm (6.7 and 1.5 W m⁻² K⁻¹ respectively). We do not have
559 good estimates of the heat flux feedback in the Southern Ocean. Frankignoul et al. (2004) find
560 that λ_F is typically about 15-20 W m⁻² K⁻¹ at the local scale in the mid-latitudes but tends
561 to decrease significantly at the basin scale (~ 10 W m⁻² K⁻¹) in the North Atlantic/Pacific.
562 It is expected to decrease further at the global scale of the SO. Again, zonal asymmetries in
563 CCSM3.5 probably contribute to the difference between the two models, enhancing air-sea
564 contrast and damping rates as air parcels move above the Southern Ocean. Cloud and sea
565 ice feedbacks are also likely contributors. Despite the factor of 4 difference between the
566 CCSM3.5 and MITgcm heat flux feedback, neither can be ruled out as unrealistic. Thus,
567 it appears that the air-sea heat interactions (forcing and damping) are significantly more
568 intense in CCSM3.5 than in the MITgcm.

569 *c. Response of the interior ocean*

570 The Frankignoul and Hasselmann (1977) model is modified by ocean interior dynamics
571 in our simple model. In the limit $t \ll \lambda_{sub}^{-1}$, the SST response (8) becomes:

$$T' \simeq \frac{\tilde{F}}{\lambda}(1 - e^{-\lambda t}) - \frac{\Lambda_e}{\lambda} w'_{res} \partial_z \bar{T}_{sub} t. \quad (10)$$

572 The time t_r at which the SST changes sign, $T'(t_r) = 0$, then depends on λ but no longer on
573 λ_{sub} . Further assuming $\lambda^{-1} \ll t \ll \lambda_{sub}^{-1}$, t_r simplifies to:

$$t_r \simeq \frac{1}{\Lambda_e} \frac{-\tilde{F}}{-w'_{res} \partial_z \bar{T}_{sub}} = \frac{1}{\Lambda_e} \frac{v'_{res} \partial_y \bar{T} - F'_a}{-w'_{res} \partial_z \bar{T}_{sub}} \quad (11)$$

574 Note that the above expression does not apply well to the CCSM3.5 case where t_r is only a
575 factor 2 smaller than λ_{sub} . Nonetheless, Eq. (11) points to the key role of residual circulation
576 in driving the change of sign. The larger v'_{res} the longer the transition (through a larger
577 initial cooling of SST) while the larger w'_{res} the shorter the transition (through increases

578 of the subsurface warming rate). As pointed out in Eq. (4) (and Fig. 11), the residual
 579 upwelling flow results from a cancellation (by a factor δ) of the wind-driven upwelling by
 580 the (parameterized) eddy-induced downwelling. However, the cancellation of the Ekman
 581 horizontal flow by the eddy-induced circulation is relatively weak in comparison with that
 582 of the vertical flow. This is because the Eulerian and eddy-induced streamfunctions do not
 583 have the same vertical distribution. The Eulerian streamfunction is constant over the fluid
 584 column and decays to zero at the surface within the Ekman layer (~ 30 m), i.e. the horizontal
 585 flow is very confined vertically (Fig. 9). In contrast, the eddy induced flow near the surface
 586 is spread over a deeper layer, of about 200 m. This mismatch between the vertical scales of
 587 the two MOC components is observed in eddy-resolving simulations (see Abernathey et al.
 588 2011; Morrison and Hogg 2013) and should not be considered an erroneous effect of the Gent
 589 and McWilliams eddy parameterization employed in the coupled GCMs (although the use of
 590 a tapering scheme in the GM scheme may have an influence). This suggests that $w'_{res} = \delta w'_{ek}$
 591 and $v'_{res} \simeq v'_{ek}$ is a better choice in which case:

$$t_r \simeq \frac{1}{\Lambda_e} \frac{v'_{ek} \partial_y \bar{T} - F'_a}{-\delta w'_{ek} \partial_z \bar{T}_{sub}} \quad (12)$$

592 In the limit of perfect eddy compensation ($\delta = 0$), t_r would go to infinity as there would
 593 be no subsurface upwelling and warming and the initial cold SST response would persist
 594 indefinitely. In the limit of no eddy compensation ($\delta=1$), the transition t_r would be more
 595 rapid. Eq. (12) emphasizes that the eddy processes (vertical structure, magnitude) may be
 596 key in determining the timescale of the SST reversal.

597 Finally, we point to the role of the entrainment time scale Λ_e^{-1} which modulates the
 598 imprint of the subsurface temperature onto the SST. It is shorter in CCSM3.5 than in the
 599 MITgcm, 0.4 and 1.5 yr, respectively (Table 1). The shorter CCSM3.5 timescale (promot-
 600 ing a shorter transition time t_r) could possibly be due to the shallower depth of the peak
 601 subsurface tendencies (see Fig. 11) or the use of a mixed layer scheme and higher vertical
 602 resolution. In both models however, the ratio λ/Λ_e which appears in Eq. (8), is about 0.6
 603 and the warming trend of the SST mimics that of the subsurface temperature (Fig. 13).

6. Conclusion

In this study, we have explored the ocean and sea ice response to ozone depletion in two coupled GCMs. The ozone depletion is imposed as a step function and we compute the transient response of the coupled system to this perturbation. As in other studies, the surface westerly winds shift poleward and strengthen during summer in response to ozone depletion; this atmospheric response is similar to the positive phase of the SAM.

The first key result of our study is that the SST response to this wind perturbation in the Southern Ocean has two phases (see Fig. 1 for a schematic). The fast response occurs on a monthly timescale following the SAM-like wind perturbation, but also builds up over a few years. It is mediated by mixed layer dynamics and air-sea interaction. It consists of a dipole, with a cooling south of the ACC (where the surface wind increases) and a warming where surface westerly winds weaken (around 35°S) (Fig. 1, left). This response is primarily driven by anomalous Ekman advection with air-sea heat interactions acting as a damping. The slow response is due to interior ocean dynamics. The northward Ekman flow at $70\text{-}50^{\circ}\text{S}$ drives upwelling south of the ACC which brings warm water to the surface. At these latitudes where sea ice expands seasonally, the water column is stratified by salinity and cold water at the surface lies over warm water below. On long (multi-year) time scales, this warmth can be entrained into the mixed layer and counteracts the initial SST cooling (Fig. 1, right). Eventually, the SST response to ozone depletion is a widespread warming of the SO.

The second key result of our study is that there is no inconsistency between inferences based on SAM/SST correlations and modeling studies of the SO response to ozone depletion. Sigmond and Fyfe (2010) and Bitz and Polvani (2012) found that ozone depletion drives a warming of the SO and sea ice loss in coupled GCMs. The SST/sea ice signatures of the positive phase of the SAM, however, suggest that ozone depletion through its surface wind impact should generate a SST cooling around Antarctica and a sea ice expansion (Goosse et al. 2009). These two conclusions are reconciled within one framework by our results showing a two-timescale response to ozone depletion.

631 Finally, a related overall outcome is that ozone depletion could drive a transient expansion
632 of the sea ice cover around Antarctica that could have contributed to the observed sea ice
633 expansion of the last 3 decades (Parkinson and Cavalieri 2012). In both GCMs used here,
634 the initial sea ice response to an abrupt ozone depletion is one of expansion, followed by a
635 contraction of the sea ice cover as the surface warms. This long term response is consistent
636 with findings by Sigmond and Fyfe (2010) and Bitz and Polvani (2012)). However, the true
637 (time-varying) influence of ozone depletion on the sea ice extent will critically depend on the
638 timescale of the transition from cooling to warming. One expects that in a model with a short
639 transition timescale such as CCSM3.5, prescribing the time-history of the ozone depletion
640 would not result in a significant sea ice expansion (consistent with results of Smith et al.
641 (2012), albeit obtained with CCSM4). On the contrary, in a model with a long transition
642 timescale such as the MITgcm, a transient SST cooling and sea ice expansion is obtained in
643 response to the historical variations of the ozone hole (work in progress).

644 An important corollary of this study is that analysis of the relationship between sea ice
645 cover and SAM changes in observations may require more sophisticated tools than previ-
646 ously used in the literature (e.g. simultaneous correlations or trends). In a recent study,
647 for example, Simpkins et al. (2012) computed the sea ice cover trends that are linearly con-
648 gruent with the SAM during summer. To do this, they regressed sea ice anomalies onto
649 the detrended SAM index, and then multiplied the resulting regression coefficients by the
650 trend in the SAM. Such an approach effectively assumes that there is a single relationship
651 between SAM and sea ice cover changes that applies on all times scales, or, equivalently that
652 there is only one (fast) timescale response. Simpkins et al. (2012) (and others, see references
653 therein) found, using such congruency analysis, that the SAM trends explain less 15% of the
654 observed sea ice trends. This is not surprising in the light of our results: we do not expect
655 that the simultaneous (3-month averaged) relationship between SAM and sea ice cover would
656 capture their relationship on long multidecadal trends. Therefore, we argue that such low
657 congruency obtained in observations does not rule out a dynamical link between SAM and

658 sea ice trends of the past 3 decades. A more accurate exploration of the SAM-sea ice link
659 needs to account for the two-timescale response.

660 Although the two-timescale SST response is a robust result seen in the two GCMs stud-
661 ied here and the mechanisms of this response are largely similar in the two GCMs, the
662 timescale of the transition between the cold and warm SST phases around Antarctica is
663 poorly constrained, being 20 years in the MITgcm and 3-5 years in CCSM3.5.

664 Two main sources of uncertainties have been identified: the nature of the air-sea in-
665 teraction and the response of the interior ocean. Air-sea heat fluxes are partly driven by
666 atmospheric changes (notably changes in wind and cloud effects) and partly by rates of
667 damping of the SST anomaly once it is created. Parameterized mesoscales eddies control
668 the effective rate of subsurface warming by partially canceling the wind-driven upwelling.
669 We emphasize that in both GCMs, eddy processes are parameterized. Eddy-resolving simu-
670 lations have shown that such cancellation is difficult to capture in parameterization schemes
671 (e.g. Hallberg and Gnanadesikan 2006; Abernathey et al. 2011). More studies are required to
672 better quantify these processes, to constrain the transition timescale using coupled GCMs,
673 process studies and observations.

674 Despite the above caveats, our results robustly demonstrate that the Southern Ocean
675 responds to wind on multiple timescales, reconciling previously contradicting views. Impor-
676 tantly, regardless of the true timescale of transition between the fast and slow phases, our
677 results highlight the need to revise the classical model of extratropical air-sea interactions
678 for the Southern ocean to account for the interior ocean dynamics.

679 *Acknowledgments.*

680 DF was supported in part by a NASA MAP grant. JM, SS and AP obtained partial
681 support from a NSF FESD project on the impact of the ozone hole on the Southern Hemi-
682 sphere climate. Funding for CB was provided by the National Science Foundation (NSF
683 PLR-1341497).

APPENDIX

684

685

The MITgcm

686

687 All components use the same cubed-sphere grid at a low resolution C24, yielding a reso-
688 lution of 3.75° at the equator (Adcroft et al. 2004). The cubed-sphere grid avoids problems
689 associated with the converging meridian at the poles and ensures that the model dynamics
690 at the poles are treated with as much fidelity as elsewhere.

691 The atmospheric physics is of ‘intermediate’ complexity, based on the “SPEEDY” scheme
692 (Molteni 2003) at low vertical resolution (5 levels, one in the stratosphere, three in the tro-
693 posphere and one in the boundary layer). Briefly, it comprises a 4-band radiation scheme, a
694 parametrization of moist convection, diagnostic clouds and a boundary layer scheme. The 3-
695 km deep, flat-bottomed ocean model has 15 vertical levels, increasing from 30 m at the surface
696 to 400 m at depth. The background vertical diffusion is uniform and set to $3 \times 10^{-5} \text{ m}^2 \text{ s}^{-1}$.

697 The sea-ice model is based on Winton (2000)’s two and a half layer thermodynamic
698 model with prognostic ice fraction, snow and ice thickness (employing an energy conserving
699 formulation). The land model is a simple 2-layer model with prognostic temperature, liquid
700 ground water, and snow height. There is no continental ice. The seasonal cycle is represented
701 (with a 23.5° obliquity and zero eccentricity) but there is no diurnal cycle.

702 Finally, as discussed by Campin et al. (2008), the present coupled ocean-sea ice-atmosphere
703 model achieves perfect (machine-accuracy) conservation of freshwater, heat and salt during
704 extended climate simulation. This is made possible by the use of the rescaled height coordi-
705 nate z^* (Adcroft and Campin 2004) which allows for a realistic treatment of the sea ice-ocean
706 interface. This property is crucial to the fidelity and integrity of the coupled system. The
707 set-up is identical to that used in Ferreira et al. (2010, 2011) and very similar to that of
708 Marshall et al. (2007) and Enderton and Marshall (2009) (see Ferreira et al. (2010) for key

709 differences).

710

711

REFERENCES

712 Abernathey, R., J. Marshall, and D. Ferreira, 2011: The dependence of southern ocean
713 meridional overturning on wind stress. *J. Phys. Oceanogr.*, **41**, 2261–2278.

714 Adcroft, A., J. Campin, C. Hill, and J. Marshall, 2004: Implementation of an atmosphere-
715 ocean general circulation model on the expanded spherical cube. *Mon. Wea. Rev.*, **132**,
716 2845–2863.

717 Adcroft, A. and J.-M. Campin, 2004: Re-scaled height coordinates for accurate representa-
718 tion of free-surface flows in ocean circulation models. *Ocean Modell.*, **7**, 269–284.

719 Bitz, C. M. and L. M. Polvani, 2012: Antarctic climate response to stratospheric ozone
720 depletion in a fine resolution ocean climate model. *Geophys. Res. Lett.*, **39**, L20 705.

721 Bryan, F. O., P. R. Gent, and R. Tomas, 2013: Can southern ocean eddy effects be param-
722 eterized in climate models? *J. Climate*, submitted.

723 Campin, J.-M., J. Marshall, and D. Ferreira, 2008: Sea ice-ocean coupling using a rescaled
724 vertical coordinate z^* . *Ocean Modell.*, **24**, 1–14.

725 Ciasto, L. M. and D. W. J. Thompson, 2008: Observations of large-scale ocean–atmosphere
726 interaction in the southern hemisphere. *J. Climate*, **21**, 1244–1259.

727 Cionni, I., et al., 2011: Ozone database in support of CMIP5 simulations: Results and
728 corresponding radiative forcing. *Atmos. Chem. Phys. Discuss.*, **11**, 10 875–10 933.

729 Comiso, J. C. and F. Nushio, 2008: Trends in the sea ice cover using enhanced and compatible
730 amsr-e, ssm/i, and smmr data. *J. Geophys. Res.*, **113**, C02S07.

731 Danabasoglu, G. and J. Marshall, 2007: Effects of vertical variations of thickness diffusivity
732 in an ocean general circulation model. *Ocean Modell.*, **18**, 122–141.

733 Dee, D. P., et al., 2011: The era-interim reanalysis: configuration and performance of the
734 data assimilation system. *Quart. J. Roy. Meteor. Soc.*, **137** (656), 553–597.

735 Enderton, D. and J. Marshall, 2009: Explorations of atmosphere-ocean-ice climates on an
736 aqua-planet and their meridional energy transports. *J. Atmos. Sci.*, **66**, 1593–1611.

737 Ferreira, D., J. Marshall, and J.-M. Campin, 2010: Localization of deep water formation:
738 role of atmospheric moisture transport and geometrical constraints on ocean circulation.
739 *J. Climate*, **23**, 1456–1476.

740 Ferreira, D., J. Marshall, and P. Heimbach, 2005: Estimating eddy stresses by fitting dy-
741 namics to observations using a residual mean ocean circulation model and its adjoint. *J.*
742 *Phys. Oceanogr.*, **35**, 1891–1910.

743 Ferreira, D., J. Marshall, and B. Rose, 2011: Climate determinism revisited: multiple equi-
744 libria in a complex climate model. *J. Climate*, **24**, 992–1012.

745 Frankignoul, C. and K. Hasselmann, 1977: Stochastic climate models. Part II: Application
746 to sea-surface temperature variability and thermocline variability. *Tellus*, **29**, 284–305.

747 Frankignoul, C., E. Kestenare, M. Botzet, A. F. Carril, H. Drange, A. Pardaens, L. Terray,
748 and R. Sutton, 2004: An intercomparison between the surface heat flux feedback in five
749 coupled models, COADS and the NCEP reanalysis. *Climate Dyn.*, **22**, 373–388.

750 Gent, P. R. and J. C. McWilliams, 1990: Isopycnic mixing in ocean circulation models. *J.*
751 *Phys. Oceanogr.*, **20**, 150–155.

752 Gent, P. R., S. G. Yeager, R. B. Neale, S. Levis, and D. A. Bailey, 2010: Improvements in
753 half degree atmosphere/land version of the CCSM. *Climate Dyn.*, **34**, 819–833.

754 Gillet, N. P. and D. W. J. Thompson, 2003: Simulation of recent southern hemisphere
755 climate change. *Science*, **302**, 273–275.

756 Goosse, H., W. Lefebvre, A. de Montety, E. Crespin, and A. H. Orsi, 2009: Consistent past
757 half-century trends in the atmosphere, the sea ice and the ocean at high southern latitudes.
758 *Climate Dyn.*, **33**, 999–1016.

759 Grise, K. M., L. M. Polvani, G. Tselioudis, Y. Wu, and M. D. Zelinka, 2013: The ozone
760 hole indirect effect: Cloud-radiative anomalies accompanying the poleward shift of the
761 eddy-driven jet in the southern hemisphere. *Geophys. Res. Lett.*, **40**, 3688–3692.

762 Hall, A. and M. Visbeck, 2002: Synchronous variability in the southern hemisphere atmo-
763 sphere, sea ice, and ocean resulting from the annular mode. *J. Climate*, **15**, 3043–3057.

764 Hallberg, R. and A. Gnanadesikan, 2006: The role of eddies in determining the structure and
765 response of the wind-driven southern hemisphere overturning: Results from the modeling
766 eddies in the southern ocean (MESO) project. *J. Phys. Oceanogr.*, **36**, 2232–2252.

767 Kiehl, J. T., T. L. Schneider, R. W. Portmann, and S. Solomon, 1999: Climate forcing due
768 to tropospheric and stratospheric ozone. *J. Geophys. Res.*, **104**, 31,239–31,254.

769 Kirtman, B. P., et al., 2012: Impact of ocean model resolution on CCSM climate simulations.
770 *Climate Dyn.*, **39**, 1303–1328.

771 Klinger, B. A., J. Marshall, and U. Send, 1996: Representation of convective plumes by
772 vertical adjustment. *J. Geophys. Res.*, **C8 (101)**, 18,175–18,182.

773 Lefebvre, W. and H. Goosse, 2008: Analysis of the projected regional sea-ice changes in the
774 southern ocean during the twenty-first century. *Climate Dyn.*, **30**, 59–76.

775 Lefebvre, W., H. Goosse, R. Timmermann, and T. Fichefet, 2004: Influence of the southern
776 annular mode on the sea-ice system. *J. Geophys. Res.*, **109**, C09 005.

777 Marshall, G. J., 2003: Trends in the southern annular mode from observations and reanalysis.
778 *J. Climate*, **16**, 4134–4143.

779 Marshall, G. J., P. A. Stott, J. Turner, W. B. Connolley, J. C. King, and T. A. Lachlan-Cope,
780 2004a: Causes of exceptional atmospheric circulation changes in the southern hemisphere.
781 *Geophys. Res. Lett.*, **31**, L14 205.

782 Marshall, J., A. Adcroft, J.-M. Campin, C. Hill, and A. White, 2004b: Atmosphere-ocean
783 modeling exploiting fluid isomorphisms. *Mon. Wea. Rev.*, **132**, 2882–2894.

784 Marshall, J., A. Adcroft, C. Hill, L. Perelman, and C. Heisey, 1997a: A finite-volume,
785 incompressible navier stokes model for studies of the ocean on parallel computers. *J.*
786 *Geophys. Res.*, **102 (C3)**, 5753–5766.

787 Marshall, J., K. C. Armour, J. R. Scott, Y. Kostov, U. Hausmann, D. Ferreira, T. G.
788 Shepherd, and C. M. Bitz, 2014: The ocean’s role in polar climate change: asymmetric
789 arctic and antarctic responses to greenhouse gas and ozone forcing. *Phil. Trans. R. Soc.*
790 *A.*, **In press**.

791 Marshall, J., D. Ferreira, J. Campin, and D. Enderton, 2007: Mean climate and variability
792 of the atmosphere and ocean on an aquaplanet. *J. Atmos. Sci.*, **64**, 4270–4286.

793 Marshall, J., C. Hill, L. Perelman, and A. Adcroft, 1997b: Hydrostatic, quasi-hydrostatic,
794 and nonhydrostatic ocean modeling. *J. Geophys. Res.*, **102 (C3)**, 5733–5752.

795 Marshall, J. and T. Radko, 2003: Residual mean solutions for the antarctic circumpolar
796 current and its associated overturning circulation. *J. Phys. Oceanogr.*, **33**, 2341–2354.

797 Molteni, F., 2003: Atmospheric simulations using a GCM with simplified physical

798 parametrizations. I: model climatology and variability in multi-decadal experiments. *Cli-*
799 *mate Dyn.*, **64**, 175–191.

800 Morrison, A. K. and A. M. Hogg, 2013: On the relationship between southern ocean over-
801 turning and acc transport. *J. Phys. Oceanogr.*, **43**, 140–148.

802 Parkinson, C. L. and D. J. Cavalieri, 2012: Antarctic sea ice variability and trends, 1979–
803 2010. *The Cryosphere*, **6**, 871–880.

804 Polvani, L. M., D. W. Waugh, G. J. P. Correa, and S.-W. Son, 2011: Stratospheric ozone
805 depletion: the main driver of twentieth-century atmospheric circulation changes in the
806 southern hemisphere. *J. Climate*, **24**, 795–812.

807 Previdi, M. and L. M. Polvani, 2014: Climate system response to stratospheric ozone deple-
808 tion and recovery. *Quart. J. Roy. Meteor. Soc.*

809 Redi, M. H., 1982: Oceanic isopycnal mixing by coordinate rotation. *J. Phys. Oceanogr.*,
810 **12**, 1154–1158.

811 Sallée, J. B., K. G. Speer, and S. R. Rintoul, 2010: Zonally asymmetric response of the
812 southern ocean mixed-layer depth to the southern annular mode. *Nature Geoscience*, **3**,
813 273–279.

814 Sen Gupta, A. and M. H. England, 2006: Coupled ocean-atmosphere-ice response to varia-
815 tions in the southern annular mode. *J. Climate*, **19**, 4457–4486.

816 Sigmond, M. and J. C. Fyfe, 2010: Has the ozone hole contributed to increased antarctic
817 sea ice extent? *Geophys. Res. Lett.*, **37**, L18 502.

818 Sigmond, M. and J. C. Fyfe, 2014: The antarctic sea ice response to the ozone hole in climate
819 models. *J. Climate*, **27**, 1336–1342.

820 Sigmond, M., J. C. Fyfe, and J. F. Scinocca, 2010: Does the ocean impact the atmospheric
821 response to stratospheric ozone depletion? *Geophys. Res. Lett.*, **37**, L12 706.

822 Simpkins, G. R., L. M. Ciasto, D. W. J. Thompson, and M. H. England, 2012: Seasonal
823 relationships between large-scale climate variability and antarctic sea ice concentration.
824 *J. Climate*, **25**, 5451–5469.

825 Smith, K. L., L. M. Polvani, and D. R. Marsh, 2012: Mitigation of 21st century antarctic
826 sea ice loss by stratospheric ozone recovery. *Geophys. Res. Lett.*, **39**, L20 701.

827 Solomon, S., R. W. Portmann, and D. W. J. Thompson, 2007: Contrast between antarctic
828 and arctic ozone depletion. *Proc. Natl. Acad. Sci.*, **104** (2), 445–449.

829 Son, S.-W., et al., 2010: Impact of stratospheric ozone on southern hemisphere circulation
830 change: A multimodel assessment. *J. Geophys. Res.*, **115** (D3(16)), D00M07.

831 Thompson, D. W. J. and S. Solomon, 2002: Interpretation of recent southern hemisphere
832 climate change. *Science*, **296**, 895–899.

833 Thompson, D. W. J., S. Solomon, P. J. Kushner, M. H. England, K. M. Grise, and D. J.
834 Karoly, 2011: Signatures of the antarctic ozone hole in southern hemisphere surface climate
835 change. *Nature Geoscience*.

836 Turner, J., et al., 2009: Non-annular atmospheric circulation change induced by stratospheric
837 ozone depletion and its role in the recent increase of antarctic sea ice extent. *Geophys.*
838 *Res. Lett.*, **36**, L08 502.

839 Watterson, I. G., 2000: Southern midlatitude zonal wind vacillation and its interaction with
840 the ocean in gcm simulations. *J. Climate*, **13**, 562–578.

841 Winton, M., 2000: A reformulated three-layer sea ice model. *J. Atmos. Oceanic Technol.*,
842 **17**, 525–531.

843 Zwally, H. J., J. C. Comiso, C. L. Parkinson, D. J. Cavalieri, and P. Gloersen, 2002: Vari-
844 ability of antarctic sea ice 1979–1998. *J. Geophys. Res.*, **107**, 3041.

845 List of Tables

846 1 Parameters of the simple model estimated by fitting Eqs. (8) and (9) to the
847 SST and subsurface temperature time series diagnosed in the MITgcm and
848 CCSM3.5 ($h_s=30$ m). The model time series and fitted curves are shown
849 in Fig. 13. The temperatures responses are averaged over 70-50°S for the
850 MITgcm and over the initial cold SST response for CCSM3.5. Note that
851 λ_F and \tilde{F}_F are the same physical quantities as λ and \tilde{F} but expressed in
852 $\text{W m}^{-2} \text{K}^{-1}$ and W m^{-2} respectively, assuming a mixed layer depth h_s of
853 30 m for both models.

36

TABLE 1. Parameters of the simple model estimated by fitting Eqs. (8) and (9) to the SST and subsurface temperature time series diagnosed in the MITgcm and CCSM3.5 ($h_s=30$ m). The model time series and fitted curves are shown in Fig. 13. The temperatures responses are averaged over 70-50°S for the MITgcm and over the initial cold SST response for CCSM3.5. Note that λ_F and \tilde{F}_F are the same physical quantities as λ and \tilde{F} but expressed in $\text{W m}^{-2} \text{K}^{-1}$ and W m^{-2} respectively, assuming a mixed layer depth h_s of 30 m for both models.

	Air-sea damping		Atm. forcing		λ_{sub}^{-1}	Λ_e^{-1}	$-w'_{res} \partial_z \bar{T}_{sub}$
	λ^{-1} year	λ_F $\text{W m}^{-2} \text{K}^{-1}$	\tilde{F} $^{\circ}\text{C year}^{-1}$	\tilde{F}_F W m^{-2}	year	year	
MITgcm	2.6	1.5	-0.18	-0.7	78	1.5	0.014
CCSM3.5	0.59	6.7	-0.27	-1.1	6.8	0.36	0.027

854 List of Figures

- 855 1 Schematic of the two-timescale response of the ocean and sea ice to an abrupt
856 ozone depletion, capturing the common features of the two GCMs: (left) the
857 fast response, similar to the signature of the interannual SAM seen in obser-
858 vations, is dominated by the surface dynamics and (right) the slow response,
859 seen in coupled GCMs, is driven by the ocean interior dynamics. Black arrows
860 denote anomalous ocean currents. Red/blue arrows denote heat fluxes in/out
861 of the surface mixed layer (marked by a thick dashed line). Blue patches rep-
862 resent the sea ice cover (expanding in the fast response and contracting in the
863 slow response). The thin dashed lines mimic the structure of isotherms in the
864 Southern Ocean, showing in particular the temperature inversion found south
865 of the ACC. Small vertical displacements (~ 10 m) of these isotherms (not
866 represented in the schematic) generate temperature anomalies in the ocean
867 interior. 40
- 868 2 Response of the geopotential height at 500 mb (in meters) to an abrupt ozone
869 depletion: (left) in DJF and (right) zonal mean climatological response for
870 (top) the MITgcm and (bottom) CCSM3.5. The time average is over the first
871 20 years. 41
- 872 3 Annual- and zonal-mean response of the surface wind stress (N m^{-2}) to an
873 abrupt ozone depletion in the MITgcm (dashed) and in CCSM3.5 (dashed-
874 dotted). The time average is over the first 20 years. For comparison, the
875 difference in surface wind stress between pre-ozone hole conditions (1980-
876 1989) and peak ozone hole conditions (1995-2004) is shown in solid, from the
877 ERA-Interim re-analysis. The vertical lines indicate the locations of the peak
878 mean surface wind stress. 42

- 879 4 Response of (left) SST ($^{\circ}\text{C}$) and surface wind (m s^{-1}) and (right) potential
880 temperature at 170 m averaged over years 1-5 (top) and 16-20 (bottom) after
881 “Ozone Hole” inception in the MITgcm. 43
- 882 5 Zonal mean SST response (monthly means, in $^{\circ}\text{C}$) in (top) the MITgcm and
883 (bottom) CCSM3.5. In the bottom panel, the vertical line separates the first
884 32 months when 20 ensemble members are averaged from the later months
885 where just 6 ensemble members are averaged. 44
- 886 6 Time evolution of the annual-mean ensemble-mean SST response (red) in
887 (left) the MITgcm and (right) CCSM3.5. Solid lines correspond to an average
888 between 70° and 50°S . In addition, for CCSM3.5, an average over the area
889 occupied by the cold pole of the first year response (see Fig. 12 top, below) is
890 shown with dash-dotted lines. The solid black line indicates the mean of the
891 best fitted curves while the grey shading denotes uncertainties (see text for
892 details). For the MITgcm, a 20 member-ensemble is used over the 40 years.
893 For CCSM3.5, a 20-member ensemble mean is only available for the first 3
894 years, after which only the ensemble mean comprises 6 members. 45
- 895 7 Total sea ice area response (in 10^6 km^2) as a function of time in summer
896 (January-March, red) and winter (August-October, black) in (left) the MIT-
897 gcm and (right) CCSM3.5. Note that CCSM3.5 starts in September, so the
898 first winter is an average of September-October only. 46
- 899 8 Response of zonal mean SST ($^{\circ}\text{C}$, red), net air-sea flux F'_F (W m^{-2} , solid black)
900 and horizontal advection at the surface $-\rho_o c_p h_s v'_{res} \partial_y \bar{T}$ (W m^{-2} , dashed-
901 dotted black) with $h_s=30 \text{ m}$. Fluxes are counted positive if they result in
902 an SST increase. Results are shown for the MITgcm experiment on the left
903 (averaged over years 2-3) and on the right for CCSM3.5 (averaged over months
904 5-28). Note the different vertical scales in the two panels. 47

- 905 9 (Top) Annual mean surface wind stress response (N m^2). (bottom) Annual
906 mean Eulerian MOC response (Sv, black) and potential temperature distri-
907 bution in the control run ($^{\circ}\text{C}$, color). The responses are averaged over years
908 6-10. 48
- 909 10 (a)-(c): Residual-mean MOC response (black) and potential temperature re-
910 sponse (color) averaged over five year periods. The contour interval for the
911 MOC are ± 0.5 , ± 1 , ± 2 Sv, etc ... Clockwise and anticlockwise circulations
912 are denoted by solid and dashed lines, respectively. (d) Time series of po-
913 tential temperature (red) averaged over the box shown in panel a). The best
914 fit slope (dashed black) equals $0.017^{\circ}\text{C}/\text{year}$. The grey shading indicates the
915 magnitude of the fast (cold) SST response around 60°S . 49
- 916 11 (Top) Eulerian (circle) and residual-mean (cross) vertical velocities (m year^{-1})
917 averaged over the latitudinal bands dominated by upwelling (blue) and down-
918 welling (red) and (bottom) subsurface vertical advection tendencies $-w'_{res} \frac{\partial \bar{T}}{\partial z}$
919 ($^{\circ}\text{C year}^{-1}$). The left and right plots correspond to the MITgcm and CCSM3.5,
920 respectively. Note that the boundaries of the latitudinal bands (top) and
921 depths at which vertical advection peaks (bottom) vary between models as
922 indicated by insets. Note also that, in the bottom plots, the vertical scale for
923 CCSM3.5 is larger than for MITgcm. 50
- 924 12 Response of SST ($^{\circ}\text{C}$) averaged over the first year (top) and years 11-20 (bot-
925 tom) after an abrupt ozone depletion in the CCSM3.5. 51
- 926 13 Best-fit (solid blue) of Eq. (8) to the CFR of the SST evolution (red, av-
927 eraged over 70 - 50°S for the MITgcm and over the initial cold SST response
928 for CCSM3.5) in (left) the MITgcm and (right) CCSM3.5. The slow and fast
929 components of the best fit are shown in dashed lines. 52

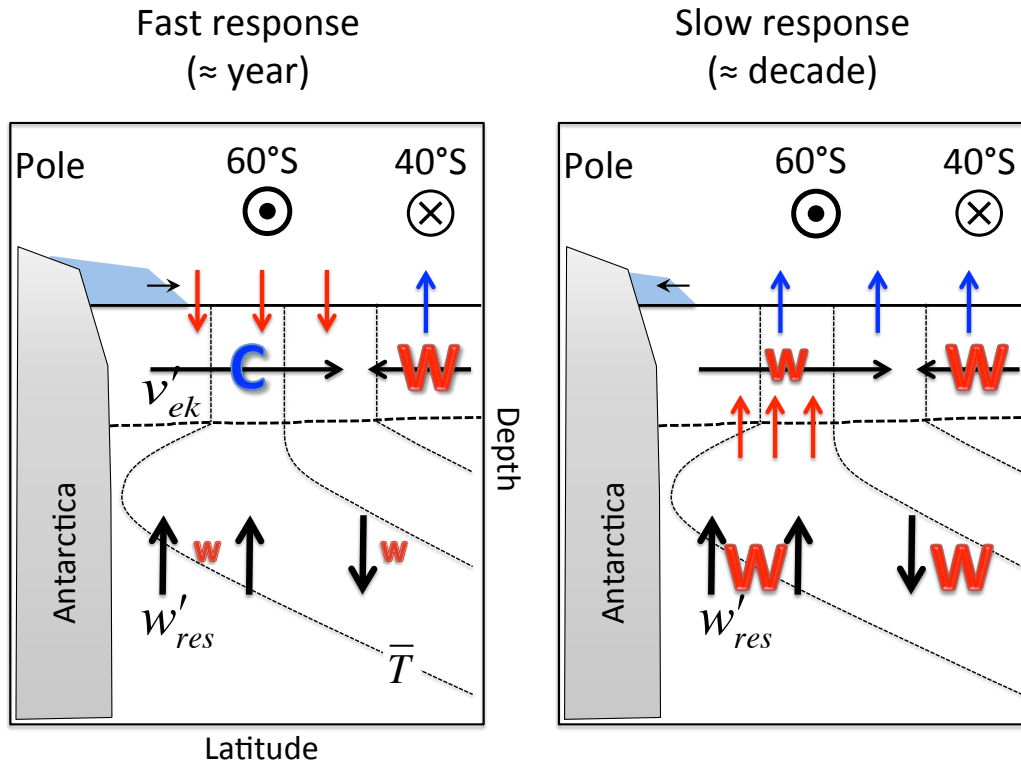


FIG. 1. Schematic of the two-timescale response of the ocean and sea ice to an abrupt ozone depletion, capturing the common features of the two GCMs: (left) the fast response, similar to the signature of the interannual SAM seen in observations, is dominated by the surface dynamics and (right) the slow response, seen in coupled GCMs, is driven by the ocean interior dynamics. Black arrows denote anomalous ocean currents. Red/blue arrows denote heat fluxes in/out of the surface mixed layer (marked by a thick dashed line). Blue patches represent the sea ice cover (expanding in the fast response and contracting in the slow response). The thin dashed lines mimic the structure of isotherms in the Southern Ocean, showing in particular the temperature inversion found south of the ACC. Small vertical displacements (~ 10 m) of these isotherms (not represented in the schematic) generate temperature anomalies in the ocean interior.

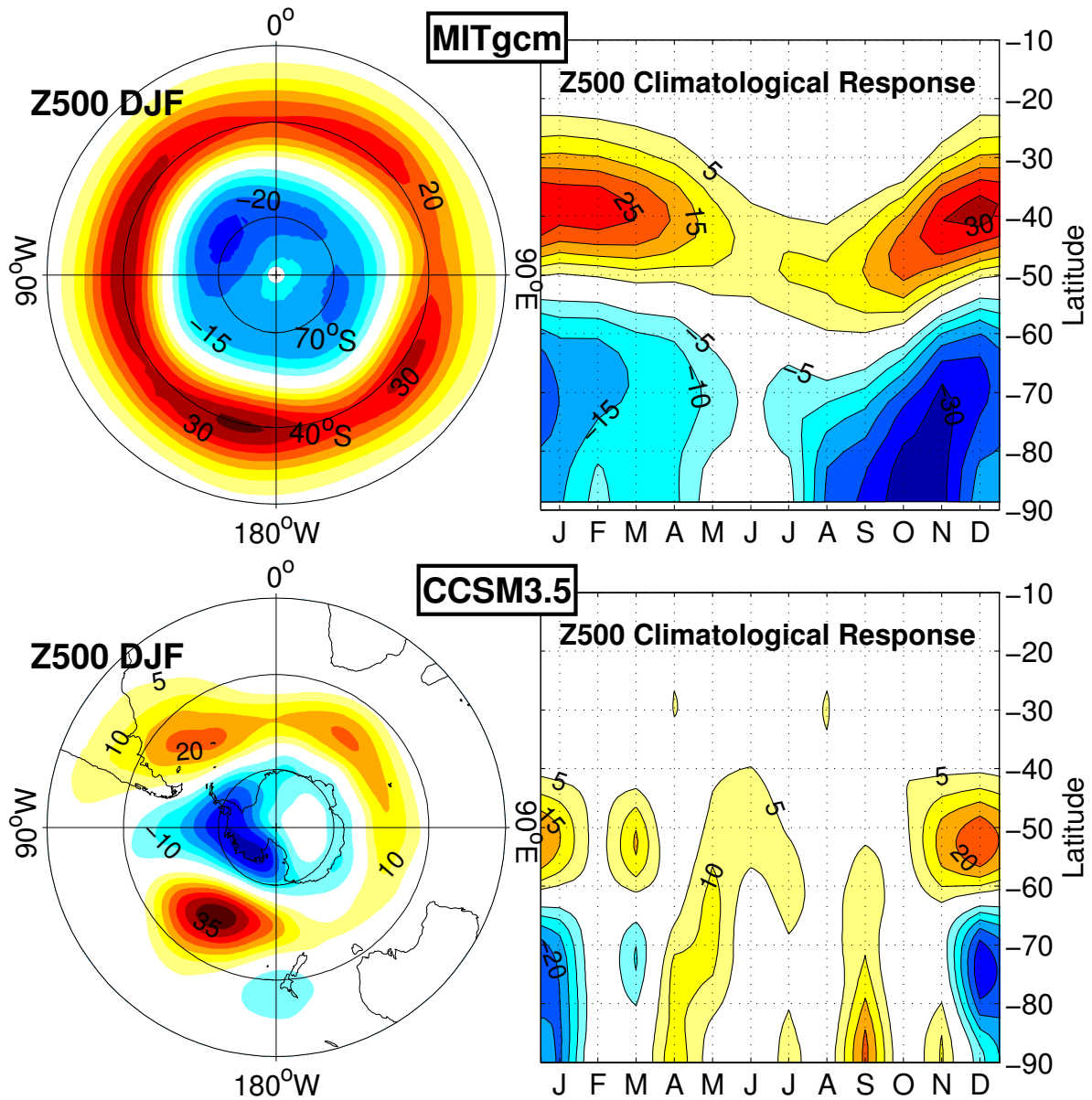


FIG. 2. Response of the geopotential height at 500 mb (in meters) to an abrupt ozone depletion: (left) in DJF and (right) zonal mean climatological response for (top) the MITgcm and (bottom) CCSM3.5. The time average is over the first 20 years.

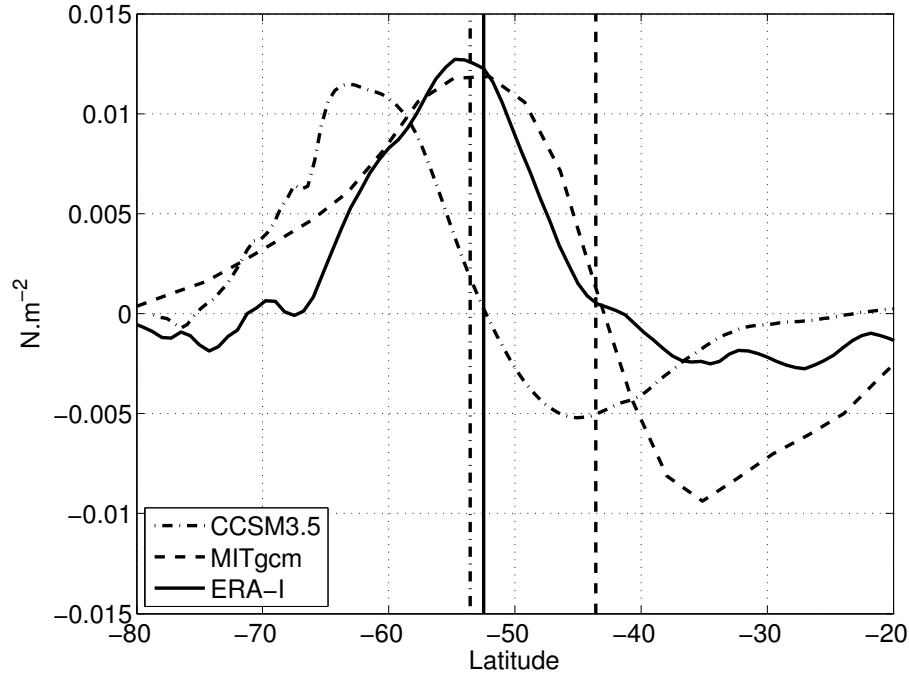


FIG. 3. Annual- and zonal-mean response of the surface wind stress (N m^{-2}) to an abrupt ozone depletion in the MITgcm (dashed) and in CCSM3.5 (dashed-dotted). The time average is over the first 20 years. For comparison, the difference in surface wind stress between pre-ozone hole conditions (1980-1989) and peak ozone hole conditions (1995-2004) is shown in solid, from the ERA-Interim re-analysis. The vertical lines indicate the locations of the peak mean surface wind stress.

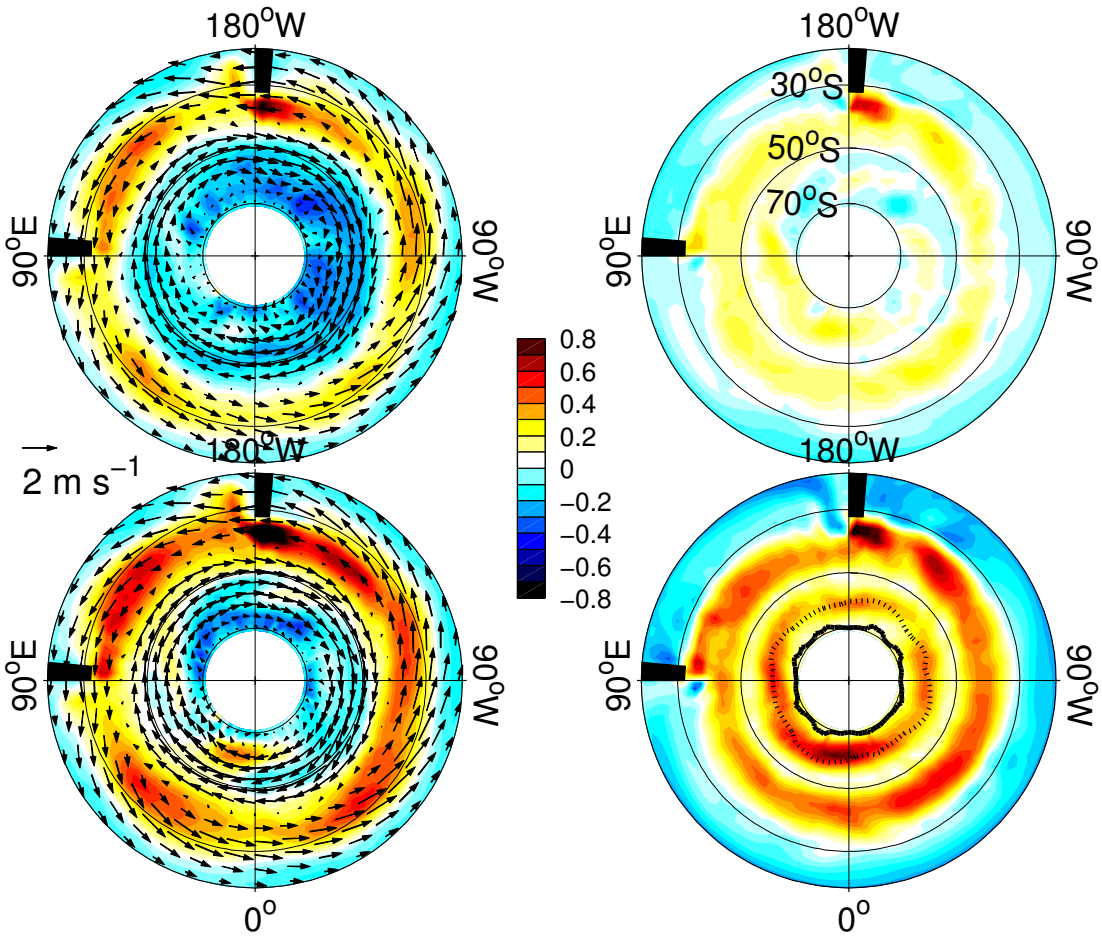


FIG. 4. Response of (left) SST ($^{\circ}\text{C}$) and surface wind (m s^{-1}) and (right) potential temperature at 170 m averaged over years 1-5 (top) and 16-20 (bottom) after “Ozone Hole” inception in the MITgcm.

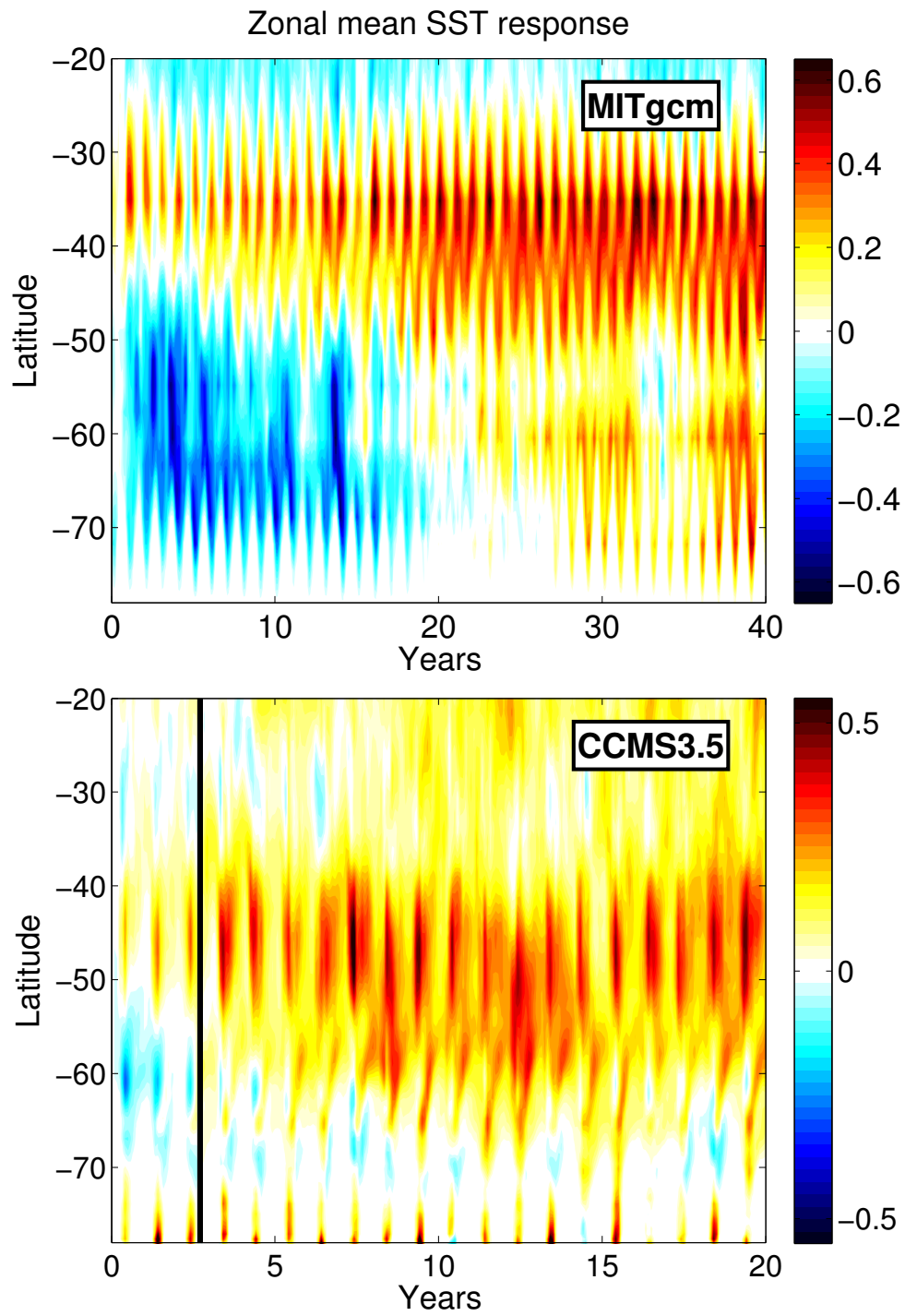


FIG. 5. Zonal mean SST response (monthly means, in $^{\circ}\text{C}$) in (top) the MITgcm and (bottom) CCSM3.5. In the bottom panel, the vertical line separates the first 32 months when 20 ensemble members are averaged from the later months where just 6 ensemble members are averaged.

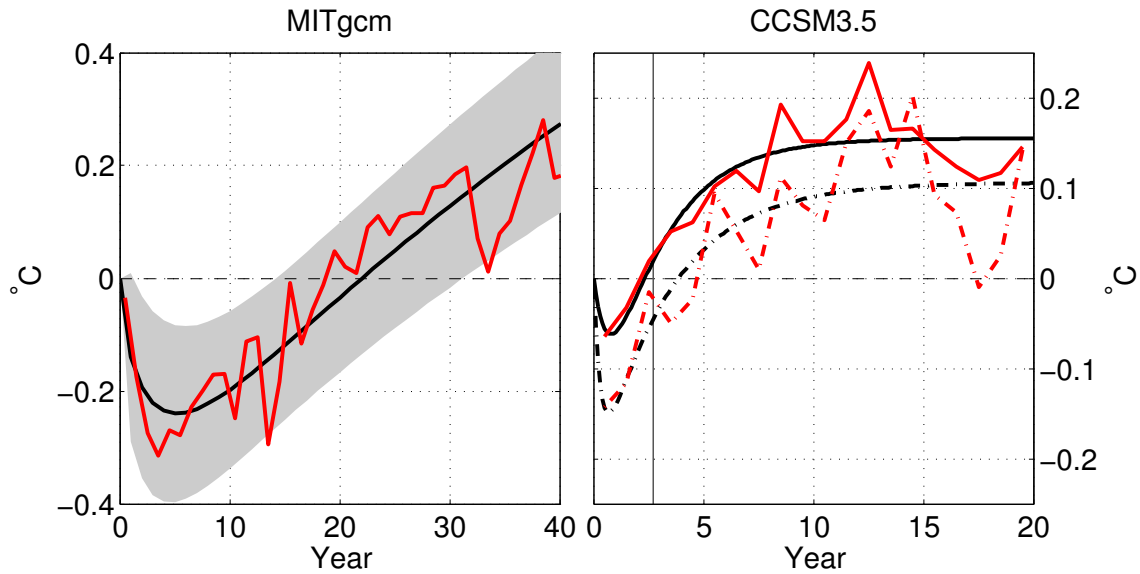


FIG. 6. Time evolution of the annual-mean ensemble-mean SST response (red) in (left) the MITgcm and (right) CCSM3.5. Solid lines correspond to an average between 70 and 50°S. In addition, for CCSM3.5, an average over the area occupied by the cold pole of the first year response (see Fig. 12 top, below) is shown with dash-dotted lines. The solid black line indicates the mean of the best fitted curves while the grey shading denotes uncertainties (see text for details). For the MITgcm, a 20 member-ensemble is used over the 40 years. For CCSM3.5, a 20-member ensemble mean is only available for the first 3 years, after which only the ensemble mean comprises 6 members.

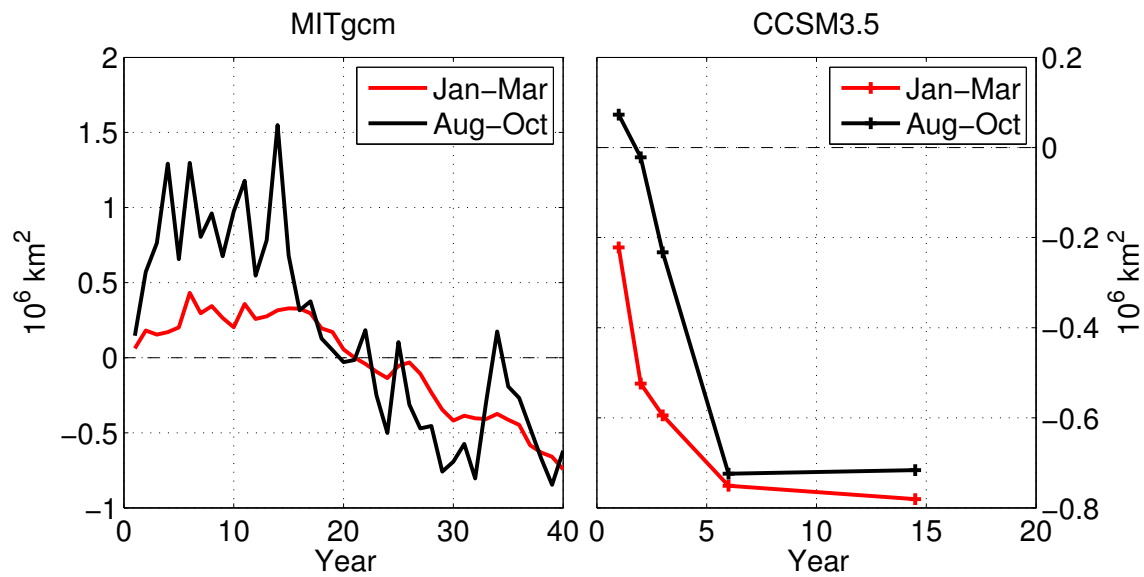


FIG. 7. Total sea ice area response (in 10^6 km^2) as a function of time in summer (January-March, red) and winter (August-October, black) in (left) the MITgcm and (right) CCSM3.5. Note that CCSM3.5 starts in September, so the first winter is an average of September-October only.

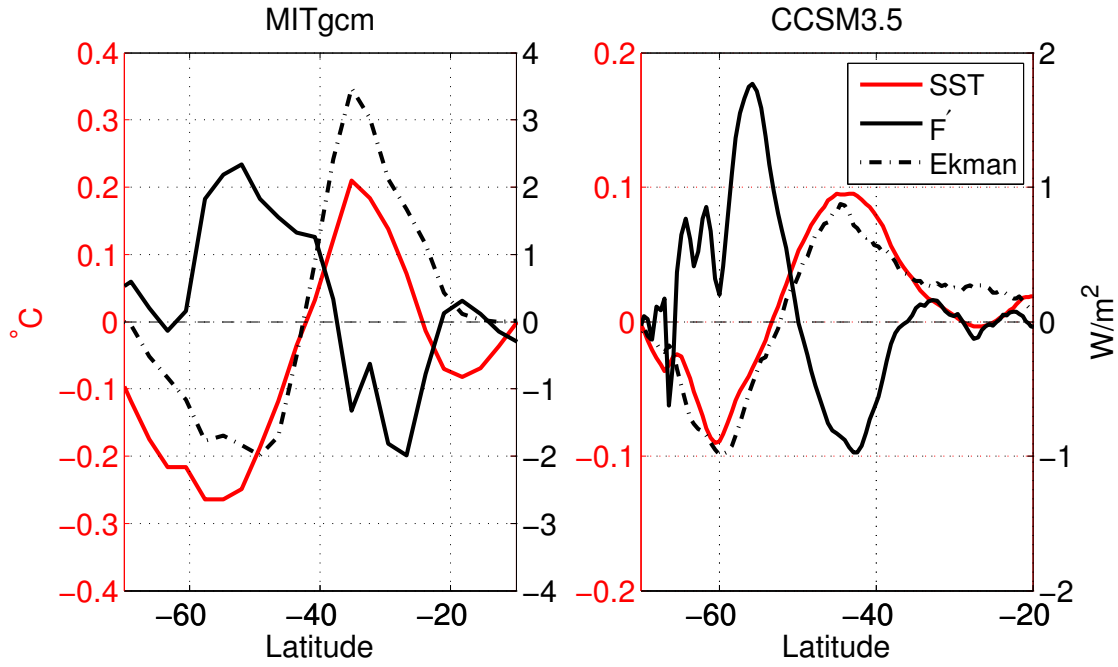


FIG. 8. Response of zonal mean SST ($^{\circ}\text{C}$, red), net air-sea flux F'_F (W m^{-2} , solid black) and horizontal advection at the surface $-\rho_o c_p h_s v'_{res} \partial_y \bar{T}$ (W m^{-2} , dashed-dotted black) with $h_s=30$ m. Fluxes are counted positive if they result in an SST increase. Results are shown for the MITgcm experiment on the left (averaged over years 2-3) and on the right for CCSM3.5 (averaged over months 5-28). Note the different vertical scales in the two panels.

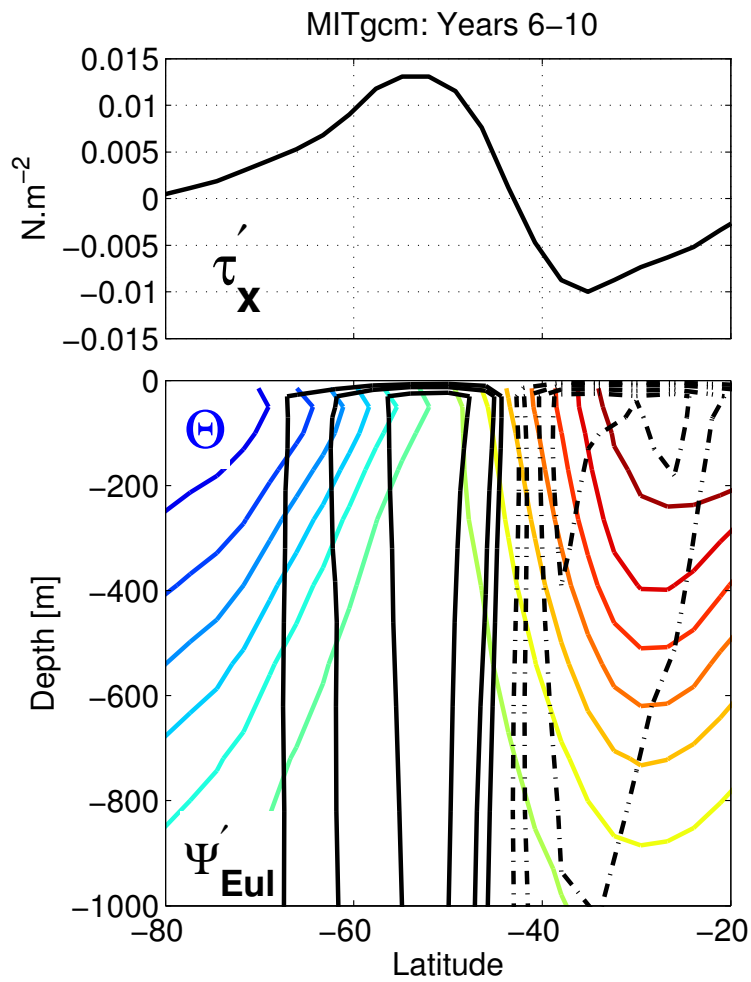


FIG. 9. (Top) Annual mean surface wind stress response (N m^2). (bottom) Annual mean Eulerian MOC response (Sv , black) and potential temperature distribution in the control run ($^{\circ}\text{C}$, color). The responses are averaged over years 6-10.

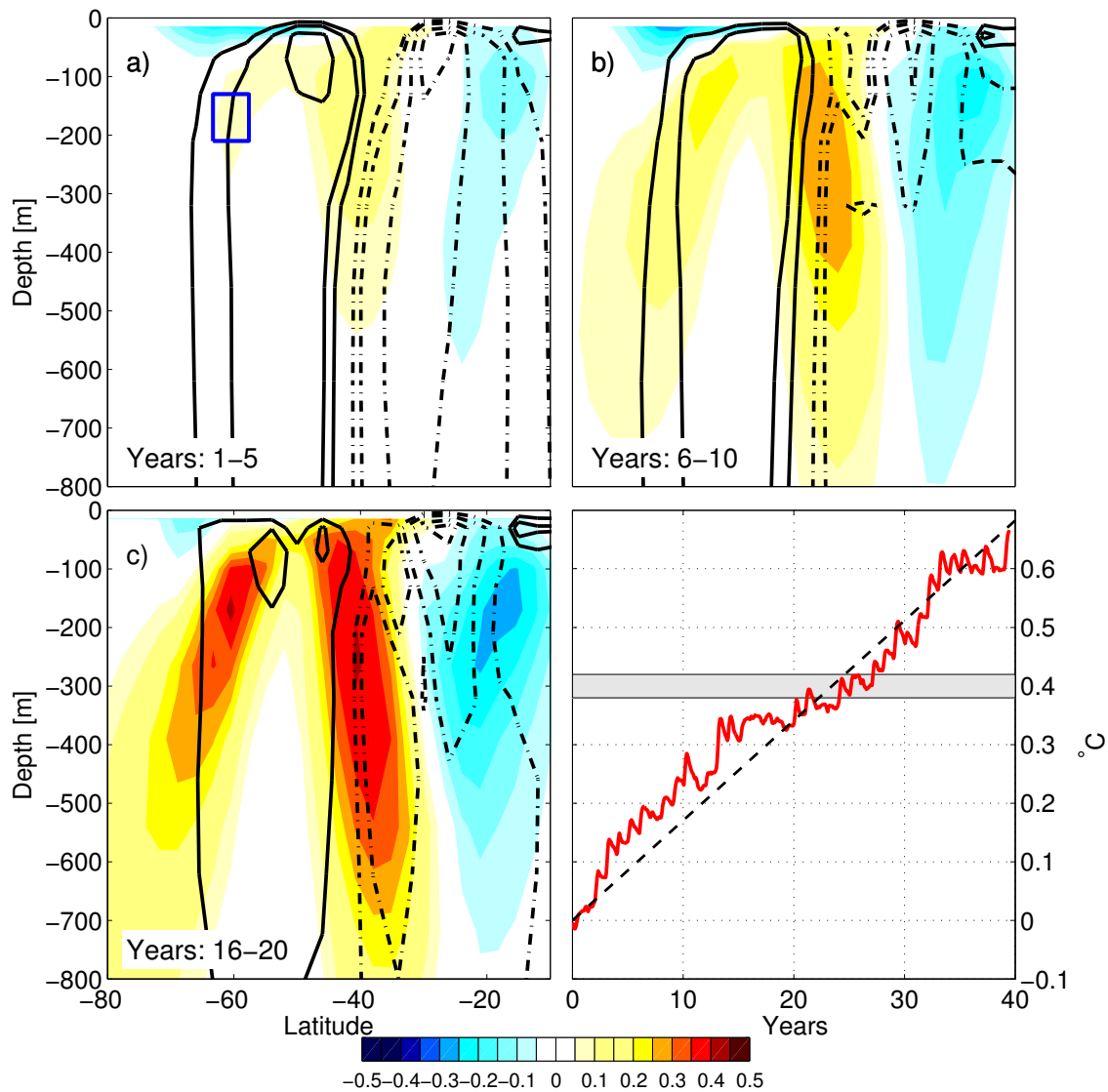


FIG. 10. (a)-(c): Residual-mean MOC response (black) and potential temperature response (color) averaged over five year periods. The contour interval for the MOC are ± 0.5 , ± 1 , ± 2 Sv, etc ... Clockwise and anticlockwise circulations are denoted by solid and dashed lines, respectively. (d) Time series of potential temperature (red) averaged over the box shown in panel a). The best fit slope (dashed black) equals $0.017^{\circ}\text{C}/\text{year}$. The grey shading indicates the magnitude of the fast (cold) SST response around 60°S .

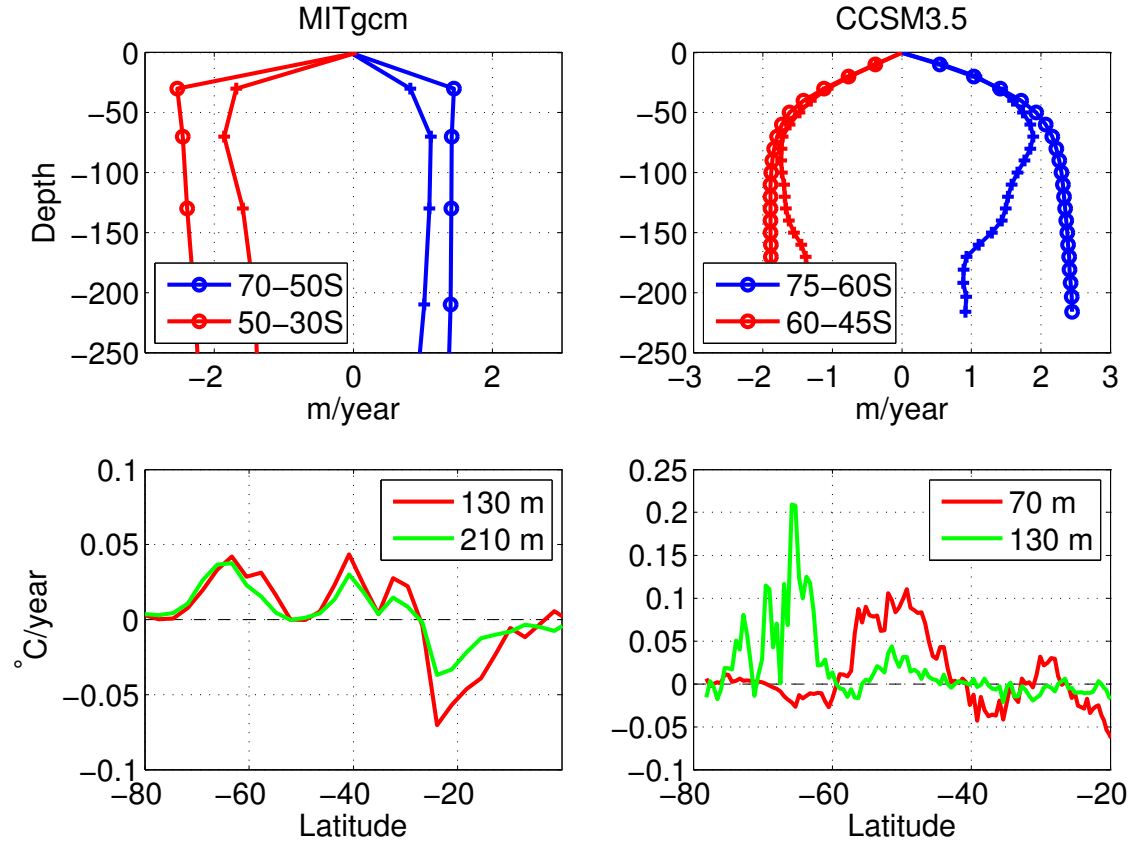


FIG. 11. (Top) Eulerian (circle) and residual-mean (cross) vertical velocities (m year^{-1}) averaged over the latitudinal bands dominated by upwelling (blue) and downwelling (red) and (bottom) subsurface vertical advection tendencies $-w'_{res} \frac{\partial T}{\partial z}$ ($^{\circ}\text{C year}^{-1}$). The left and right plots correspond to the MITgcm and CCSM3.5, respectively. Note that the boundaries of the latitudinal bands (top) and depths at which vertical advection peaks (bottom) vary between models as indicated by insets. Note also that, in the bottom plots, the vertical scale for CCSM3.5 is larger than for MITgcm.

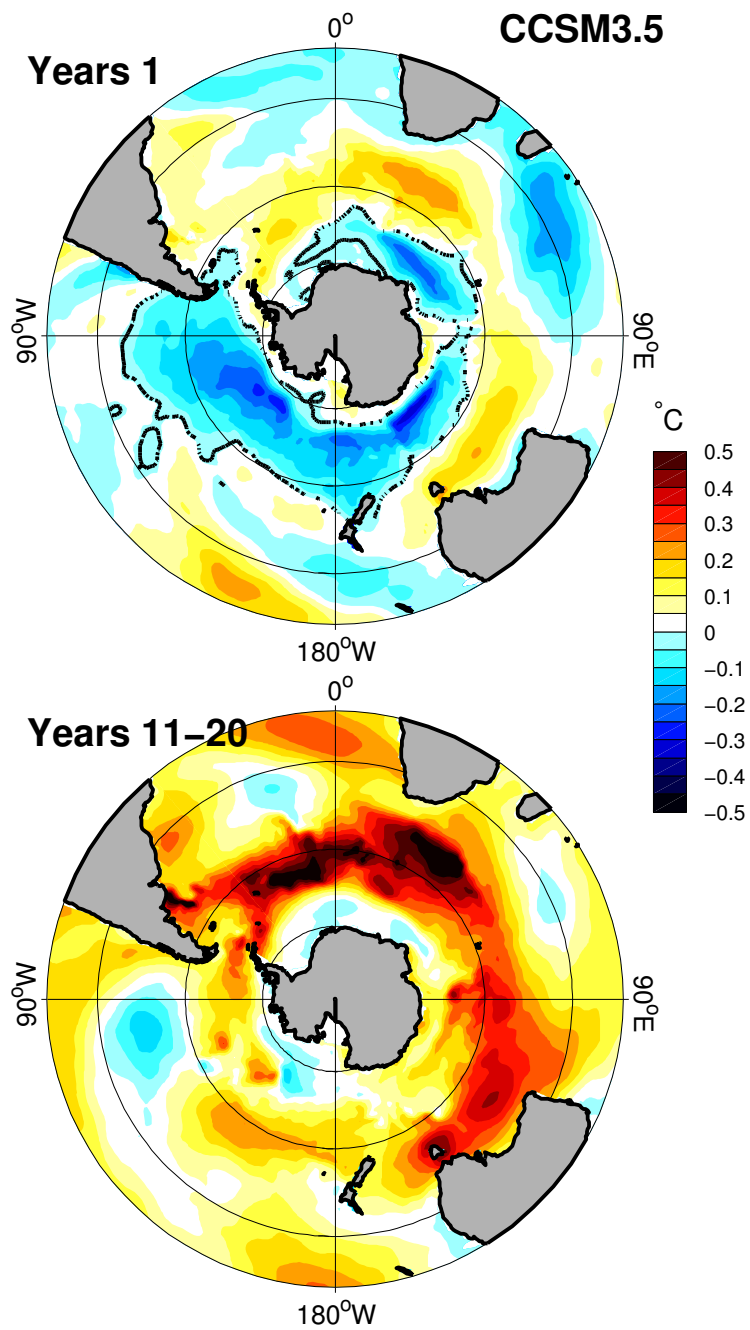


FIG. 12. Response of SST ($^{\circ}\text{C}$) averaged over the first year (top) and years 11-20 (bottom) after an abrupt ozone depletion in the CCSM3.5.

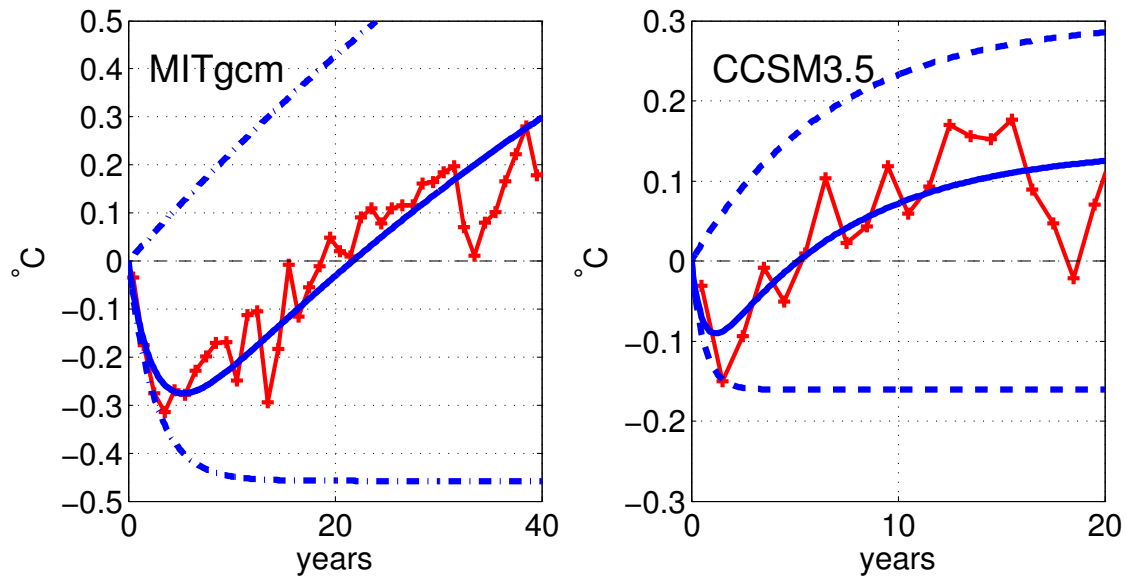


FIG. 13. Best-fit (solid blue) of Eq. (8) to the CFR of the SST evolution (red, averaged over $70\text{-}50^\circ\text{S}$ for the MITgcm and over the initial cold SST response for CCSM3.5) in (left) the MITgcm and (right) CCSM3.5. The slow and fast components of the best fit are shown in dashed lines.